HAL
open science

A tunable Fabry-Pérot quantum Hall interferometer in graphene

Corentin Déprez, Louis Veyrat, Hadrien Vignaud, Goutham Nayak, Kenji Watanabe, Takashi Taniguchi, Frédéric Gay, Hermann Sellier, Benjamin Sacépé

To cite this version:

Corentin Déprez, Louis Veyrat, Hadrien Vignaud, Goutham Nayak, Kenji Watanabe, et al.. A tunable Fabry-Pérot quantum Hall interferometer in graphene. Nature Nanotechnology, 2021, 16, pp.555-562. 10.1038/s41565-021-00847-x . hal-02997027

HAL Id: hal-02997027

https://hal.science/hal-02997027

Submitted on 9 Nov 2020

HAL is a multi-disciplinary open access archive for the deposit and dissemination of scientific research documents, whether they are published or not. The documents may come from teaching and research institutions in France or abroad, or from public or private research centers.

L'archive ouverte pluridisciplinaire **HAL**, est destinée au dépôt et à la diffusion de documents scientifiques de niveau recherche, publiés ou non, émanant des établissements d'enseignement et de recherche français ou étrangers, des laboratoires publics ou privés.

arXiv:2008.11222v1 [cond-mat.mes-hall] 25 Aug 2020

A tunable Fabry-Pérot quantum Hall interferometer in graphene

Corentin Déprez,[1] Louis Veyrat,[1] Hadrien Vignaud,[1] Goutham Nayak,[1] Kenji Watanabe,[2] Takashi Taniguchi,[3] Frédéric Gay,[1] Hermann Sellier,[1] and Benjamin Sacépé[1,*]

[1] *Univ. Grenoble Alpes, CNRS, Grenoble INP, Institut Néel, 38000 Grenoble, France*
[2] *National Institute for Materials Science, 1-1 Namiki, Tsukuba 306-0044, Japan*
[3] *International Center for Materials Nanoarchitectonics*

Electron interferometry with quantum Hall edge channels holds promise for probing and harnessing exotic exchange statistics of non-Abelian anyons. In semiconductor heterostructures, however, quantum Hall interferometry has proven challenging and often obscured by charging effects. Here we show that high-mobility monolayer graphene equipped with a series of gate-tunable quantum point contacts that act as electron beam-splitters provides a model system to perform Fabry-Pérot quantum Hall interferometry. We observe high-visibility Aharonov-Bohm interference free of charging effects and widely tunable through electrostatic gating or magnetic field, in remarkable agreement with theory. A coherence length of more than $20\,\mu m$ allows us to further achieve coherently-coupled double Fabry-Pérot interferometry, as envisioned in braiding schemes of non-Abelian anyons. Our results open a new avenue for quantum Hall interferometry and the exploitation of topological excitations for quantum computation.

The wave-like behavior of electrons is exemplified in metals and semiconductors by a variety of mesoscopic phenomena stemming from quantum interference effects. Universal conductance fluctuations in coherent conductors or quantum (weak) localization due to random scattering are some vivid examples. In two dimensional electron gases, quantum interferences can be precisely tailored and harnessed using the chiral edge channels of the paradigmatic quantum Hall (QH) effect as one-dimensional, coherent electron beams. Electrostatic manipulation and partitioning of QH edge channel trajectories via local gates and quantum point contacts (QPCs) –that is, tunable beam-splitters for electrons– makes it possible to construct on-chip electronic analogues of Fabry-Pérot[1] (FP) or Mach-Zehnder[2] optical interferometers, usable for quantum information processing[3].

Central to QH interferometry is the prospect of exploiting the non-Abelian properties of some fractional QH states for topological quantum computation[4]. Winding fractional edge excitations around localized bulk ones is the elementary process sensitive to the anyonic statistical exchange phase[5] –a quantity recently evidenced via shot-noise measurements[6]– which allows braiding of non-Abelian excitations[7–11]. This process is intrinsically realized with the topology of the Fabry-Pérot interferometer in which an edge channel, partially reflected between two QPCs, encloses localized excitations into an interfering loop (see Fig. 1). As such, the QH Fabry-Pérot configuration stands as a prominent testbed for anyonic and non-Abelian interferometry. Moreover, advanced devices based on coherently-coupled double Fabry-Pérot interferometers have been envisioned as a possible route for achieving topologically protected qubits addressable via braiding operations[8].

The body of work on QH Fabry-Pérot interferometers hitherto performed in GaAs heterostructures[12–20] is, however, facing various difficulties. Observing quantum interference tunable by gate electrodes and magnetic field through the Aharonov-Bohm effect has proven often disguised by charging effects in the Fabry-Pérot cavity[12–16,19,21]. The Coulomb blockade[22–24] that is due to the small interferometer sizes has long hindered progress by imposing demanding device architectures that implement various types of screening electrodes to mitigate charging effects[18,20]. Furthermore, the delicate edge channel reconstructions in GaAs involving neutral modes[25] or counter-propagating charge modes[26] complicates interferometry[27]. All these highlight the essential need for exploring QH interferometry in other two-dimensional electron gases.

Here, we demonstrate that graphene monolayer is a promising alternative platform for QH Fabry-Pérot interferometry, free of charging effects, thereby opening new perspectives for (non-Abelian) anyon interferometry and topological quantum computing. Graphene comes forth as an ideal two-dimensional electron gas with all necessary features: high-mobility[28], fractional quantum Hall effect[29,30] with large energy gaps[31], including possible non-Abelian states[32,33], helical edge channels at charge neutrality[34,35], gate-tunability, and versatility of van der Waals heterostructures[36]. Similarely with the graphene bilayer[37–39].

Yet, gate tunable QPCs –the key component to construct elaborated QH interferometers– has proven challenging to realize due to the gapless band structure of graphene. Depleting the electron gas through electrostatic gating accumulates holes and yields conducting pn-junctions[40] that short-circuit QPC constrictions[41]. Other alternatives involve partitioning at a pn junctions[42,43], or etched constrictions[44] that yield devices subject to charging effects. We remedy this with the use of high-mobility graphene in the QH regime for which an insulating, broken-symmetry state develops and opens an energy gap at the charge neutrality point separating the conduction band from the valance band[34]. This gap is essential for the functioning of split gates as full-fledged QPC with tunable edge channel transmission[45]: It suppresses some possible charge transfers at the pn junction

surrounding the split-gates (see drawing in Fig. 2d).

We thus devised our device on the basis of a high-mobility graphene van der Waals heterostructure made with an hexagonal boron nitride (hBN)-encapsulated graphene monolayer[46] resting atop a graphite flake that acts as a back-gate electrode. As depicted in Fig. 1a, three pairs of split-gates of 20 nm gap, on top of the heterostructure, serve as QPCs and define a double FP cavity. Plunger gates located on the edges of each cavity are used to move the trajectory of the interfering QH edge channel and modulate the effective interferometer areas. The device we focus on in this report is shown in Fig. 1b with QPCs highlighted in red and labeled QPC_1, QPC_2 and QPC_3, plunger gates in orange and ohmic contacts in yellow (see Supp. Section III for the design characteristics of the QPC geometry). This triple QPC configuration enables us to operate three FP interferometers that we denote small (QPC_2-QPC_3), medium (QPC_1-QPC_2) and large (QPC_1-QPC_3) interferometers, whose geometrical areas are 3.1, 10.7 and 13.1 μm^2, respectively (see Supp. Table S2).

To operate the QH-FP interferometers, the graphene electron gas is subjected to a perpendicular magnetic field, B, to reach the quantum Hall regime. Prior to electron interferometry, each QPC transmission is individually characterized by mapping out the diagonal resistance R_D measured across contacts V_D^+ and V_D^- as a function of back-gate and split-gate voltages (see Supp. Fig. S5). We choose to work at bulk filling fractions $\nu_b = n_b\phi_0/B$ (n_b is the bulk charge carrier density, $\phi_0 = h/e$ is the flux quantum with h the Planck constant and e the electron charge) such that two electron-type edge channels of the zeroth Landau level propagate on the graphene edges, as indicated by a Hall conductance of $2e^2/h$ (see Supp. Fig. S7). A proper tuning of the split-gate voltages enables us to partially transmit either the inner or outer edge channel at the QPCs. Other configurations with only one electron-type edge channel present in the bulk have also been studied (see Supp. Section XII).

Widely tunable quantum interference

The quantum interferences in the small electronic Fabry-Pérot interferometer readily show up in Fig. 2a-c, which display the oscillatory behavior of the diagonal resistance R_D as a function of the plunger-gate voltage V_{pg2}. For this measurement performed at $B = 14$ T, the QH-FP interferometer operates at $\nu_b = 1.5$. We tuned QPC_2 and QPC_3 to a transmission of the outer edge channel $T_2 = 0.60$ and $T_3 = 0.68$, respectively, leaving the inner one fully backscattered and localized in the FP cavity (see Supp. Fig. S6 for the QPCs transmission curves). In this configuration, R_D oscillates with 50% visibility (see Fig. 2a and b) over nearly the whole voltage range spanned by the plunger gate (Fig. 2c), starting around $V_{pg2} = -0.3$ V down to $V_{pg2} = -4$ V. Further oscillations extending to positive V_{pg2} values when electrons are accumulated beneath the plunger gate are shown in Supp. Fig. S8. These results showing more than 280 resistance oscillations demonstrate the high stability and wide tunability of our interferometer.

The oscillatory behavior of the diagonal resistance upon depleting the electron gas beneath the plunger gate is a direct consequence of the modulation δA of the interferometer area defined by the interfering edge channel. Changing the flux through the interferometer via δA yields a variation $\delta\varphi = 2\pi B\delta A/\phi_0$ of the Aharonov-Bohm phase picked up by the electrons. The flux-modulated succession of constructive and destructive electron wave-function interferences is thus reflected in the stark oscillations of the diagonal resistance.

Plunger-gate electrostatics

Inspecting the oscillations more closely on a smaller span around two different plunger-gate voltages, $V_{pg2} = -3$ V and -1 V in Fig. 2a and b, respectively, we see that the period depends upon the plunger-gate voltage. This behavior can be tracked by computing the Fourier transform restricted to a small voltage window sliding over the entire V_{pg2} range. The resulting Fourier amplitude shown in Fig. 2e as a function of V_{pg2} and plunger-gate-voltage frequency f_{pg2} displays a single peak that disperses to lower frequency upon decreasing V_{pg2} to more negative values. This is consistent with the larger periodicity observed in Fig. 2a with respect to that of Fig. 2b. Notice that a second harmonic indicated by the black arrow in the inset of Fig. 2e is also visible, mostly at large negative V_{pg2}.

The V_{pg2}-dispersion of the oscillations frequency reflects the electrostatics of the plunger gate. Depleting the graphene electron gas and then accumulating hole states locally under the plunger gate repels the interfering edge channel towards the interior of the QH-FP interferometer as illustrated in the schematics in Fig. 2d, therefore reducing the effective area. The abrupt drop of the oscillation frequency f_{pg2} at $V_{pg2} \simeq -0.3$ V corresponds to the expulsion out of the area beneath the plunger gate of the interfering edge channel that was initially propagating along the graphene edge. This expulsion occurs when the graphene beneath the plunger gate reaches charge neutrality (or filling fraction 1 for the inner edge channel interfering case, see Fig. 2d). For more negative V_{pg2}, f_{pg2} decreases more slowly due to the accumulation of holes and the ensuing displacement of the pn-junction further away from the plunger gate.

The plunger gate tuning of the magnetic flux is demonstrated by the magnetic field dependence of the oscillations period. The area variation $\Delta A = \phi_0/B$ that yields a change of one flux quantum in the interferometer relates to the plunger-gate voltage period ΔV_{pg2} by $\Delta A = \alpha\Delta V_{pg2}$, where α is the (non-linear) lever arm of the gate. As $f_{pg2} = 1/\Delta V_{pg2}$, the quantity $f_{pg2}/B = \alpha/\phi_0$ depends only on the electrostatic displacement of the pn interface that is encoded in α. Fig. 2f displays f_{pg2}/B as a function of $\bar{V}_{pg2}$, gathered from Fig. 2e and from similar data obtained at $B = 11$ and

8 T, and also by making interfering the inner edge channel through a suitable tuning of the QPCs (see Supp. Fig. S9). Here, $\bar{V}_{\mathrm{pg2}}$ is the plunger-gate voltage shifted with respect to the voltage that expels the inner or outer edge channel. Despite a large variation of magnetic field, and hence of oscillations periods, all data collapse onto the same curve, confirming the flux periodicity.

Furthermore, this data collapse draws the $\bar{V}_{\mathrm{pg2}}$-evolution of the lever arm, which can be directly compared to numerical simulations of the electrostatic displacement of the pn junction in our device geometry (see Supp. Fig. S10). The resulting computation of α/ϕ_0 shown by the black line in Fig. 2f consistently fits the data and therefore demonstrates the ϕ_0-periodicity of the oscillations, bearing out the Aharonov-Bohm origin of the resistance oscillations.

Aharonov-Bohm effect vs Coulomb blockade

A critical aspect of QH-FP interferometers lies in the possibility that the resistance oscillations result from charging effects in the FP cavity[22–24], instead of Aharonov-Bohm quantum interference. Thorough studies on this issue showed that these two competing phenomena can be straightforwardly differentiated by the magnetic-field dependence of the gate-induced oscillations[13,15,19,23,24]: For the Aharonov-Bohm effect, resistance oscillations in the B–V_{pg} plane shall draw diagonal lines of negative slope, indicating constant flux $\phi = B\delta A + A\delta B$ through the interferometer, whereas a zero or positive slope is expected for the Coulomb blockade effect. This led us to perform systematic measurements of the resistance oscillations as a function of plunger-gate voltage and magnetic-field variation δB. Figure 3 displays two typical resistance maps obtained with the small interferometer (Fig. 3a) and with the large one (Fig. 3b), both at $B = 14$ T with the outer edge channel interfering. For both cases, resistance maxima (minima) draw lines of negative slope: Upon increasing magnetic field the lines go to more negative values of V_{pg}, hence shrinking the area to maintain the Aharonov-Bohm phase (flux) constant. This behavior that we constantly observed in all configurations, regardless of the interferometer size, magnetic field value, bulk filling factor being 1 or 2, or which edge channel is interfering (see Supp. Section VIII), definitely rules out the alternative Coulomb blockade scenario.

The absence of Coulomb blockade even in the smaller interferometer, whose dimensions are similar to those in GaAs devices that exhibit Coulomb blockade[13], points to a specificity of the hBN-graphene heterostructure. For our device, a source of charging effect mitigation is the close proximity of the graphite back gate. Yet, we also observed Aharonov-Bohm interference in two other graphene devices equipped instead with a 285 nm thick SiO_2 back-gate dielectric (see Supp. Section XII), which is about 16 times less efficient in screening, indicating that another effect is at play. We conjecture that the remarkable absence of Coulomb blockade can be accounted for by the ambipolar nature of graphene and the ensuing accumulation of hole states beneath QPC split gates. The pn interface surrounding the split gates forms an insulating barrier due to the interaction-induced $\nu = 0$ energy gap, but since the spatial separation between the electron and hole states that co-propagate on both sides of the pn interface is relatively small, the resulting capacitance of the pn junction is large. The pn junctions therefore provide large capacitive couplings between the FP cavity and the localized hole states, and subsequently to the rest of the graphene flake. The relevant charging energy is in turn reduced. This unique situation is in stark contrast with GaAs FP interferometers for which QPC split gates fully deplete the electron gas, isolating the FP cavity from the leads.

The magnetic-field period ΔB of the Aharanov-Bohm oscillations provides a direct measure of the effective area A_{AB} drawn by the interfering edge channel. For the three interferometers we obtained $\Delta B = 1.32$, 0.40 and 0.27 mT corresponding to $A_{AB} = 3.1$, 10.4 and 15.0 $\mu\mathrm{m}^2$, which is consistent with our expected geometrical areas of 3.1 ± 0.4, 10.7 ± 1.2 and 13.1 ± 1.8 $\mu\mathrm{m}^2$, substantiating the ϕ_0-periodicity obtained with the electrostatic analysis of the plunger-gate effect. Notice that the precision of the geometrical areas is limited by the uncertainty in the optical determination of the graphene physical edges position, which could easily explain the small differences with the measured Aharonov-Bohm areas.

Decoherence and thermal broadening

The loss of visibility in QH interferometers is a fundamental question that encompasses several phenomena such as thermal broadening or quantum decoherence by inelastic processes and energy relaxation. We investigated the coherence properties of our interferometers through the joint analysis of the bias and temperature dependence of the visibility. The multiple QPCs configuration enables us to systematically study the coherence properties for three different cavity lengths. We begin with the out-of-equilibrium measurements performed with a dc voltage bias V_{dc} applied on the source contact (the drain contact is kept grounded). Electrons injected at a finite energy $\delta\epsilon$ above the Fermi energy of the cavity have a phase shift $2\pi\delta\epsilon 2L/hv$ proportional to twice the length L of the edge channel between the two QPCs and to the edge-excitation velocity v. This additional phase shift adds up to the Aharonov-Bohm phase yielding theoretically a variety of oscillation patterns as a function of magnetic flux and voltage bias, which depend on the voltage drop across the device[5]. For a symmetric drop at the two QPCs ($V_{\mathrm{dc}}/2$ and $-V_{\mathrm{dc}}/2$ on the source and drain), the resistance oscillations draw a checkerboard pattern of the form $\delta R_{\mathrm{D}} \propto \cos(2\pi\phi/\phi_0)\cos(2\pi eV_{\mathrm{dc}}/E_{\mathrm{Th}})$. For a fully asymmetric drop (V_{dc} and 0 on the source and drain) a diagonal strip pattern of the form $\delta R_{\mathrm{D}} \propto \cos(2\pi\phi/\phi_0 - 4\pi eV_{\mathrm{dc}}/E_{\mathrm{Th}})$ is expected instead. In these expressions, the oscillations

period as a function of $V_{\rm dc}$ is governed by the ballistic Thouless energy $E_{\rm Th} = h/\tau$ related to the traveling time $\tau = L/v$ between the two QPCs[5,24].

For the large interferometer at $B = 14$ T, the resistance oscillations at finite bias (Fig. 3d) draw a checkerboard pattern similar to those observed in GaAs devices[14,20,47]. The resulting oscillations decay quickly as a function of the dc voltage $V_{\rm D}^{\rm dc}$ (measured across the diagonal contacts $V_{\rm D}^{+}$ and $V_{\rm D}^{-}$), indicating that some energy relaxation processes are at play at finite bias (see Supp. Fig. S18). Repeating the measurements on the two other interferometers yields similar patterns (see Supp. Section XIV), though with a notable difference in the form of the checkerboard which tends to be tilted towards a diagonal strip pattern upon reducing the interferometer size, as illustrated in Fig. 3c for the small interferometer. This tilt can be accounted for by an incomplete equilibration of chemical potential carried by the electron flow, which partially maintains the asymmetric voltage drop across the cavity. Calculation of the theoretical FP transmission[5] with an unbalanced voltage drop describes very well the observed tilted checkerboard, as shown in Fig. 3e and f (theoretical analysis and additional data are provided in Supp. Section XIV).

The key parameter extracted from these checkerboards is the Thouless energy of the cavity $E_{\rm Th} = hv/L$ that is given by the $V_{\rm D}^{\rm dc}$-periodicity. The resulting values shown in Fig. 3i for the three interferometers are found to consistently scale with $1/L$.

Besides, theory predicts that the temperature dependence of the oscillations visibility also relates to the Thouless energy[5]. The blurring of interference by the thermal broadening of the impinging electrons leads to an exponential suppression of the visibility with temperature, which follows $\exp(-4\pi^2 k_{\rm B}T/E_{\rm Th})$ with $k_{\rm B}$ the Boltzmann constant. In Fig. 3g and h we show the T-dependence of the resistance oscillations for the three interferometers. A clear exponential suppression of the visibilities is obtained in all cases, which is fitted with $\exp(-T/T_0)$ (dashed lines in Fig. 3h). The resulting $4\pi^2 k_{\rm B}T_0$ values that we append to Fig. 3i conspicuously scale as $1/L$ and are furthermore in excellent agreement with the Thouless energies extracted from the checkerboard patterns, bearing out a visibility limited by thermal broadening. The slope in Fig. 3i further enables us to extract an estimate of the edge velocity $v = 1.4 \times 10^5$ m.s^{-1}, which is of the same order as that obtained in GaAs devices[14,20,48], though here at a much higher magnetic field. Finally, the coherence length can be assessed with the data of the largest interferometer for which the resistance oscillations emerge below 0.065 K (see Fig. 3h). We thus obtain a lower bound of 20 μm (twice the cavity length, $2L$) for the coherence length at $T \simeq 0.065$ K. This global set of data that complies with most of the theoretical expectations[5] therefore demonstrates graphene to be a highly tunable, model platform for QH-FP interferometry.

Coherently-coupled double FP interferometer

A prerequisite for manipulating the degenerate ground state manifold formed by a set of non-Abelian anyons is the ability to spatially move non-Abelian quasiparticles around localized ones[4]. Starting from a single cavity QH-FP interferometer, this can be achieved by adding a third QPC to form two coherently-coupled FP cavities into which non-Abelian quasiparticles are localized in each cavity forming entangled pairs. A braiding operation consists then in transferring, sequentially, quasiparticles from one edge to the other through the central QPC, resulting in a parity change of the degenerate ground state, which can be read out via the interference signal[4,8]. Similar ideas have been developed for Majorana zero modes in superconductor-proximitized semiconducting nanowires, though with different manipulation and readout schemes[49].

Here we operate our device in a three QPCs configuration to show that the large FP interferometer remains coherent upon turning on backscattering at the middle QPC. As sketched in Fig. 4a and b, Aharonov-Bohm interference depends upon three fluxes, $\phi_{1,2,3}$, defined by the three cavity areas (blue, green and yellow in Fig. 4b, respectively). Each of them can be tuned by the magnetic field and one or two plunger gates. Figure 4c displays the resistance of the device for the three QPCs tuned at partial transmission of the outer edge channel, with a total transmission $T \simeq 0.46$, upon varying both plunger-gate voltages $V_{\rm pg1}$ and $V_{\rm pg2}$. The resistance oscillates with both gate voltages, drawing a regular pattern characteristic of the flux variation ϕ_1 with $V_{\rm pg1}$ (blue FP cavity), and ϕ_2 with $V_{\rm pg2}$ (green FP cavity). Coherence through the double interferometer is unveiled in the 2D Fourier transform in Fig. 4e. In addition to the two peaks at frequencies $(f_{\rm pg1}, f_{\rm pg2}) = (53\,{\rm V}^{-1}, 0\,{\rm V}^{-1})$ and $(0\,{\rm V}^{-1}, 60\,{\rm V}^{-1})$ corresponding to fluxes ϕ_1 and ϕ_2 respectively, a third peak emerges at $(f_{\rm pg1}, f_{\rm pg2}) = (53\,{\rm V}^{-1}, 60\,{\rm V}^{-1})$, indicative of a joint modulation by both plunger gates and hence a modulation of the double cavity flux ϕ_3. This peak is the result of the interference process for which electron wavefunctions interfere coherently after passing twice (back and forth) through the partially-transmitting middle QPC.

Figure 4d shows a complementary measurement where the magnetic field is varied together with the plunger-gate voltage $V_{\rm pg2}$ acting on the area of the small interferometer. We observe diagonal stripes similar to those in Fig. 3a and characteristic of the Aharonov-Bohm effect for the small cavity with flux ϕ_2 (see peak at $(f_B, f_{\rm pg2}) = (0.79\,{\rm mT}^{-1}, 90\,{\rm V}^{-1})$ in Fig. 4f), but with an additional wiggling. This wiggling result from the Aharonov-Bohm oscillations of the medium interferometer (in series with the small one) via the flux ϕ_1, which is independent of $V_{\rm pg2}$ and corresponds to the peak at $(f_B, f_{\rm pg2}) = (2.54\,{\rm mT}^{-1}, 0\,{\rm V}^{-1})$ in the Fourier transform (see Fig. 4f). The double cavity flux ϕ_3, which depends upon both B and $V_{\rm pg2}$, leads to a peak at $(f_B, f_{\rm pg2}) = (3.49\,{\rm mT}^{-1}, 90\,{\rm V}^{-1})$ with a magnetic field

periodicity which corresponds to the double cavity area, that is, the sum of the small and medium cavity areas. The precise shape of the wiggling of the diagonal stripes is a direct evidence of the contribution of the double cavity flux (see Supp. Section XVI for an additional measurement configuration and theoretical analysis).

The observation of the flux periodicity ϕ_3 provides compelling evidence that electron interference occurs through the central QPC at partial transmission, and hence that both FP cavities are coherently coupled. Such a tunable multiple FP interferometer paves the way to more advanced devices in which sequential transfer of single particles at the central QPC, controlled for instance with an anti-dot in the QPC constriction, would enable braiding schemes for non-Abelian anyons[8].

Conclusion and outlook

Finally, the high-visibility Aharonov-Bohm interference that we observe with unprecedented agreement with the non-interacting theory[5] demonstrates the relevance of graphene for performing prototypical QH-FP interferometry with integer quantum Hall edge channels. The high mobility and the versatility of the graphene van der Waals hetereostructures turn out to be pivotal to harness fine control of QH edge-channel transmissions in QPCs[45], and therefore construct advanced gate-tunable interferometers. With further study in the fractional quantum Hall regime, this graphene platform gives new opportunities for anyon physics in QH interferometers, potentially extendable to time-resolved electron quantum optics experiments[3]. Besides, the recent advances in coupling graphene QH edge channels with superconductivity[50–52] may lead to a variety of novel interferometry devices[53] in which proximity-induced topological superconductivity could be intertwined with QH interferometry for readout or braiding schemes. Such perspectives could in turn open alternative pathways for quantum-information processing of topological excitations[54–56].

* Corresponding author : benjamin.sacepe@neel.cnrs.fr

1 van Wees, B. J. *et al.* Observation of zero-dimensional states in a one-dimensional electron interferometer. *Phys. Rev. Lett.* **62**, 2523–2526 (1989).

2 Ji, Y. *et al.* An electronic mach-zehnder interferometer. *Nature* **422**, 415–418 (2003).

3 Bäuerle, C. *et al.* Coherent control of single electrons: a review of current progress. *Reports on Progress in Physics* **81**, 056503 (2018).

4 Nayak, C., Simon, S., Stern, A., Freedman, M. & Das Sarma, S. Non-Abelian anyons and topological quantum computation. *Rev. Mod. Phys.* **80**, 1083–1159 (2008).

5 Chamon, C., Freed, D. E., Kivelson, S. A., Sondhi, S. L. & Wen, X. G. Two point-contact interferometer for quantum Hall systems. *Phys. Rev. B* **55**, 2331–2343 (1997).

6 Bartolomei, H. *et al.* Fractional statistics in anyon collisions. *Science* **368**, 173–177 (2020).

7 Fradkin, E., Nayak, C., Tsvelik, A. & Wilczek, F. A Chern-Simons effective field theory for the Pfaffian quantum Hall state. *Nuclear Physics B* **516**, 704 – 718 (1998).

8 Das Sarma, S., Freedman, M. & Nayak, C. Topologically Protected Qubits from a Possible Non-Abelian Fractional Quantum Hall State. *Phys. Rev. Lett.* **94**, 166802 (2005).

9 Bonderson, P., Kitaev, A. & Shtengel, K. Detecting Non-Abelian Statistics in the $\nu = 5/2$ Fractional Quantum Hall State. *Phys. Rev. Lett.* **96**, 016803 (2006).

10 Chung, S. B. & Stone, M. Proposal for reading out anyon qubits in non-Abelian $\nu = 12/5$ quantum Hall state. *Phys. Rev. B* **73**, 245311 (2006).

11 Stern, A. & Halperin, B. Proposed Experiments to Probe the Non-Abelian $\nu = 5/2$ Quantum Hall State. *Phys. Rev. Lett.* **96**, 016802 (2006).

12 Camino, F. E., Zhou, W. & Goldman, V. J. $e/3$ laughlin quasiparticle primary-filling $\nu = 1/3$ interferometer. *Phys. Rev. Lett.* **98**, 076805 (2007).

13 Zhang, Y. *et al.* Distinct signatures for Coulomb blockade and Aharonov-Bohm interference in electronic Fabry-Perot interferometers. *Phys. Rev. B* **79**, 241304 (2009).

14 McClure, D. T. *et al.* Edge-state velocity and coherence in a quantum Hall Fabry-Pérot interferometer. *Phys. Rev. Lett.* **103**, 206806 (2009).

15 Ofek, N. *et al.* Role of interactions in an electronic Fabry-Perot interferometer operating in the quantum Hall effect regime. *PNAS* **107**, 5276–5281 (2010).

16 McClure, D. T., Chang, W., Marcus, C. M., Pfeiffer, L. N. & West, K. Fabry-Perot Interferometry with Fractional Charges. *Phys. Rev. Lett.* **108**, 256804 (2009).

17 Willett, R. L., Nayak, C., Shtengel, K., Pfeiffer, L. N. & West, K. W. Magnetic-Field-Tuned Aharonov-Bohm Oscillations and Evidence for Non-Abelian Anyons at $\nu = 5/2$. *Phys. Rev. Lett.* **111**, 186401 (2013).

18 Choi, H. K. *et al.* Robust electron pairing in the integer quantum hall effect regime. *Nature Commun.* **6**, 7435 (2015).

19 Sivan, I. *et al.* Observation of interaction-induced modulations of a quantum Hall liquid's area. *Nature Commun.* **7**, 12184 (2016).

20 Nakamura, J. *et al.* Aharonov-Bohm interference of fractional quantum Hall edge modes. *Nature Physics* **15**, 563–569 (2019).

21 Röösli, M. P. *et al.* Observation of quantum Hall interferometer phase jumps due to a change in the number of bulk quasiparticles. *Phys. Rev. B* **101**, 125302 (2020).

22 Rosenow, B. & Halperin, B. I. Influence of Interactions on Flux and Back-Gate Period of Quantum Hall Interferometers. *Phys. Rev. Lett.* **98**, 106801 (2007).

23 Halperin, B., Stern, A., Neder, I. & Rosenow, B. Theory of the Fabry-Pérot quantum Hall interferometer. *Phys. Rev. B* **83**, 155440 (2011).

24 Ngo Dinh, S. & A. Bagrets, D. Influence of Coulomb interaction on the Aharonov-Bohm effect in an electronic Fabry-Pérot interferometer. *Phys. Rev. B* **85**, 073403 (2012).

25 Bid, A. *et al.* Observation of neutral modes in the fractional quantum Hall regime. *Nature* **466**, 585–590 (2010).

26 Lafont, F., Rosenblatt, A., Heiblum, M. & Umansky, V. Counter-propagating charge transport in the quantum Hall effect regime. *Science* **363**, 54–57 (2019).

27 Bhattacharyya, R., Banerjee, M., Heiblum, M., Mahalu,

D. & Umansky, V. Melting of Interference in the Fractional Quantum Hall Effect: Appearance of Neutral Modes. *Phys. Rev. Lett.* **122**, 246801 (2019).

[28] Wang, L. *et al.* One-dimensional electrical contact to a two-dimensional material. *Science* **342**, 614–617 (2013).

[29] Du, X., Skachko, I., Duerr, F., Luican, A. & Andrei, A. Y. Fractional quantum hall effect and insulating phase of dirac electrons in graphene. *Nature* **462**, 192–195 (2009).

[30] Bolotin, K. I., Ghahari, F., Shulman, M. D., Stormer, H. L. & Kim, P. Observation of the fractional quantum hall effect in graphene. *Nature* **462**, 196–199 (2009).

[31] Dean, C. R. *et al.* Multicomponent fractional quantum hall effect in graphene. *Nature Physics* **7**, 693–696 (2011).

[32] Kim, Y. *et al.* Even denominator fractional quantum Hall states in higher Landau levels of graphene. *Nature Physics* **15**, 154–158 (2018).

[33] Zibrov, A. A. *et al.* Even-denominator fractional quantum Hall states at an isospin transition in monolayer graphene. *Nature Physics* **15**, 154–158 (2018).

[34] Young, A. F. *et al.* Tunable symmetry breaking and helical edge transport in a graphene quantum spin hall state. *Nature* **505**, 528–532 (2014).

[35] Veyrat, L. *et al.* Helical quantum Hall phase in graphene on $SrTiO_3$. *Science* **367**, 781–786 (2020).

[36] Yankowitz, M., Ma, Q., Jarillo-Herrero, P. & LeRoy, B. J. van der Waals heterostructures combining graphene and hexagonal boron nitride. *Nature Reviews Physics* **1**, 112–125 (2019).

[37] Maher, P. *et al.* Evidence for a spin phase transition at charge neutrality in bilayer graphene. *Nature Physics* **9**, 154–158 (2013).

[38] Ki, D.-K., Falko, V. I., Abanin, D. A. & Morpurgo, A. F. Observation of Even Denominator Fractional Quantum Hall Effect in Suspended Bilayer Graphene. *Nano Letters* **14**, 2135–2139 (2014).

[39] Li, J. I. A. *et al.* Even-denominator fractional quantum Hall states in bilayer graphene. *Science* **358**, 648–652 (2017).

[40] Huard, B. *et al.* Transport measurements across a tunable potential barrier in graphene. *Phys. Rev. Lett.* **98**, 236803 (2007).

[41] Veyrat, L. *et al.* Low-Magnetic-Field Regime of a Gate-Defined Constriction in High-Mobility Graphene. *Nano Letters* **19**, 635–642 (2019).

[42] Wei, D. S. *et al.* Mach-Zehnder interferometry using spin- and valley-polarized quantum Hall edge states in graphene. *Science Advances* **3**, e1700600 (2017).

[43] Makk, P. *et al.* Coexistence of classical snake states and Aharonov-Bohm oscillations along graphene $p-n$ junctions. *Phys. Rev. B* **98**, 035413 (2018).

[44] Zhang, G.-Q. *et al.* Coulomb-dominated oscillations in a graphene quantum Hall Fabry–Pérot interferometer. *Chinese Physics B* **28**, 127203 (2019).

[45] Zimmermann, K. *et al.* Tunable transmission of quantum Hall edge channels with full degeneracy lifting in split-gated graphene devices. *Nature Commun.* **8**, 14983 (2017).

[46] Wang, L. *et al.* One-dimensional electrical contact to a two-dimensional material. *Science* **342**, 614–617 (2013).

[47] Yamauchi, Y. *et al.* Universality of bias- and temperature-induced dephasing in ballistic electronic interferometers. *Phys. Rev. B* **79**, 161306 (2009).

[48] Gurman, I., Sabo, R., Heiblum, M., Umansky, V. & Mahalu, D. Dephasing of an electronic two-path interferometer. *Phys. Rev. B* **93**, 121412 (2016).

[49] Alicea, J., Oreg, Y., Refael, G., Von Oppen, F. & Fisher, M. P. Non-Abelian statistics and topological quantum information processing in 1D wire networks. *Nature Physics* **7**, 412–417 (2011).

[50] Amet, F. *et al.* Supercurrent in the quantum hall regime. *Science* **352**, 966–969 (2016).

[51] Lee, G.-H. *et al.* Inducing superconducting correlation in quantum Hall edge states. *Nature Physics* **13**, 693–698 (2017).

[52] Zhao, L. *et al.* Interference of chiral Andreev edge states. *Nature Physics* **16**, 862–867 (2020).

[53] Huang, X.-L. & Nazarov, Y. V. Interaction-induced supercurrent in quantum Hall setups. *Phys. Rev. B* **100**, 155411 (2019).

[54] Clarke, D., Alicea, J. & Shtengel, K. Exotic non-Abelian anyons from conventional fractional quantum Hall states. *Nature Commun.* **4**, 1348 (2013).

[55] Stern, A. & Lindner, N. H. Topological Quantum Computation—From Basic Concepts to First Experiments. *Science* **339**, 1179–1184 (2013).

[56] Mong, R. S. K. *et al.* Universal Topological Quantum Computation from a Superconductor-Abelian Quantum Hall Heterostructure. *Phys. Rev. X* **4**, 011036 (2014).

[57] Liu, M. Theory of carrier density in multigated doped graphene sheets with quantum corrections. *Phys. Rev. B* **87**, 125427 (2013).

[58] Roulleau, P. *et al.* Finite bias visibility of the electronic Mach-Zehnder interferometer. *Phys. Rev. B* **76**, 161309 (2007).

[59] Roulleau, P. *et al.* Noise Dephasing in Edge States of the Integer Quantum Hall Regime. *Phys. Rev. Lett.* **101**, 186803 (2008).

[60] Litvin, L. V., Helzel, A., Tranitz, H.-P., Wegscheider, W. & Strunk, C. Edge-channel interference controlled by Landau level filling. *Phys. Rev. B* **78**, 075303 (2008).

METHODS

Sample fabrication

hBN/graphene/hBN heterostructures were assembled from exfoliated flakes using the van der Waals pick-up technique[46]. The substrates are highly doped Si wafers with a 285 nm thick SiO_2 layer. For the sample discussed in the main text (BNGr74), the heterostructure is deposited on a thin layer of graphite that serves as a back-gate electrode. Contacts were patterned by electron-beam lithography and metalized by e-gun evaporation of a Cr/Au bilayer after etching of the stack with a CHF_3/O_2 plasma directly through the resist pattern used to define the contacts. The electrostatic plunger and split gates were obtained with a second electron-beam lithography step and subsequent evaporation of Pd. The graphite layer for sample BNGr74 was also contacted at this step on a purposely uncovered part. Two other samples (BNGr64 and BNGr30) discussed in Supp. Section XII were prepared without graphite-gate electrode but with the hBN/graphene/hBN heterostructure resting directly atop the Si/SiO_2 substrate.

Measurements

Measurements were performed in a dilution fridge reaching a base temperature of 0.01 K and equipped with a superconducting solenoid. To ensure good electron thermalization, the fridge is equipped with room-temperature feedthrough filters, highly-dissipative wiring, copper-powder filters at the mixing chamber stage, and cryogenic-compatible capacitors to ground on each line mounted directly on the sample holder. Devices were measured in four-terminal, voltage-bias configuration using an ac voltage of 5 μV and low-frequency lock-in amplifier techniques. Current was measured with a home-made current-voltage converter. Non-linear transport measurements were carried out by adding a dc voltage between source and drain contacts and measuring the dc and ac components of the diagonal voltage V_{D}. Measurements of the resistance oscillations as a function of magnetic field and plunger-gate voltage were performed by using the current decay of the superconducting solenoid in persistent mode while sweeping the plunger-gate voltage with a 20 bits home-made voltage source. All room-temperature low-noise pre-amplifiers were thermalized in a home-made, temperature-controlled box to get rid of thermal drifts of input voltage offsets.

ACKNOWLEDGMENTS

We thank I. Aleiner for valuable discussions. We thank F. Blondelle for his technical support. Samples were prepared at the Nanofab facility of Néel Institute. This work was supported by the H2020 ERC grant *QUEST* No. 637815. K.W. and T.T. acknowledge support from the Elemental Strategy Initiative conducted by the MEXT, Japan, Grant Number JPMXP0112101001, JSPS KAKENHI Grant Number JP20H00354 and the CREST(JPMJCR15F3), JST.

COMPETING INTERESTS

The authors declare that they have no competing financial interests.

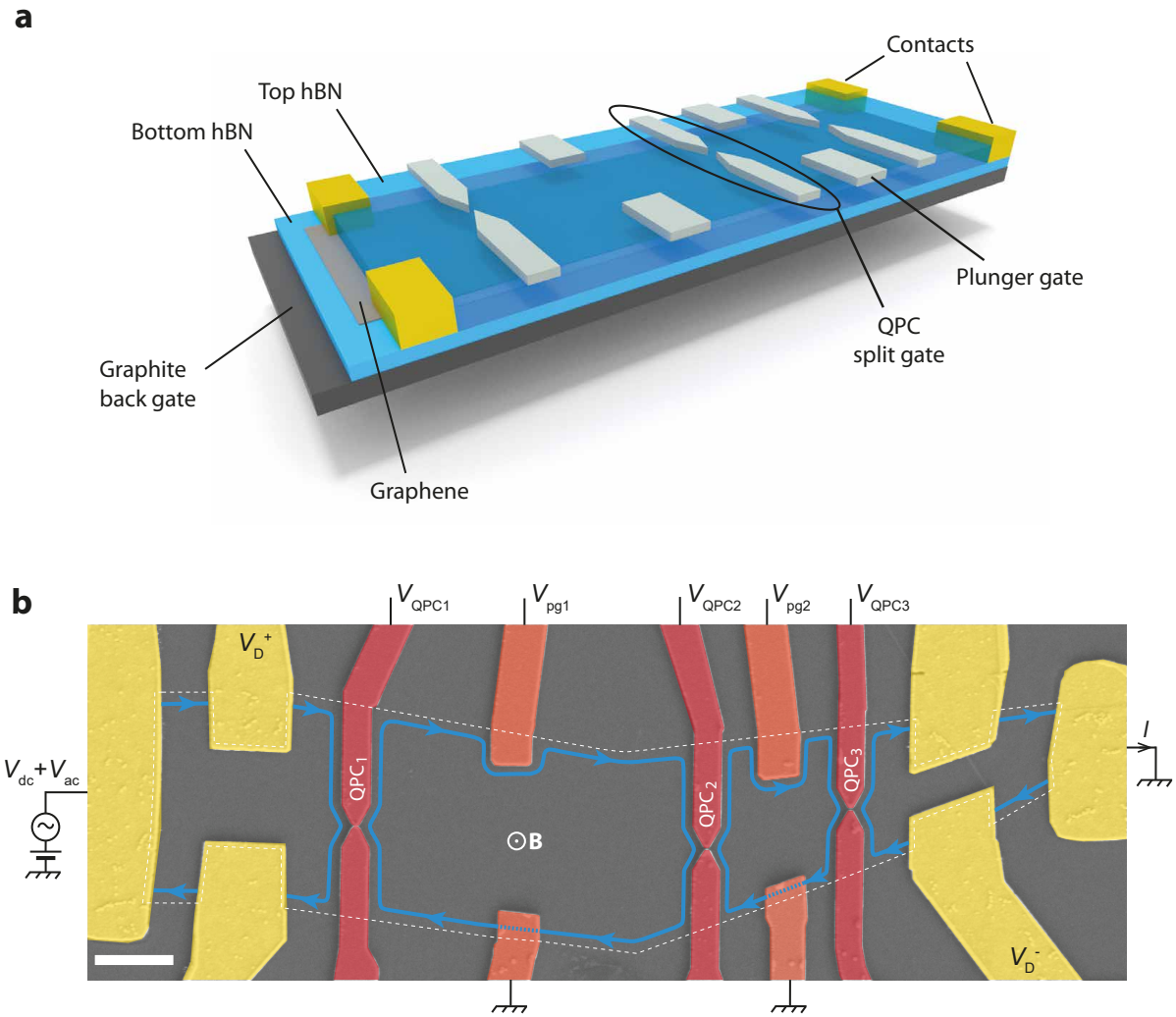

FIG. 1. **Graphene quantum Hall Fabry-Pérot interferometer.** **a,** Schematic of the van der Waals hBN/graphene/hBN/graphite heterostructure equipped with split-gate and plunger-gate electrodes (light gray) atop it. The graphite flake serves as back-gate electrode and the graphene is contacted through edge contacts[28] (yellow). Further details about nanofabrication are given in Methods. **b,** False-colored scanning electron micrograph of the device. The scale bar is 1 μm. Three QPCs define two FP cavities. The interfering quantum Hall edge channel (blue line) propagates along the graphene edges (white dashed line), and along the split-gate (red) and plunger-gate (orange) electrodes, illustrating a configuration in which the gate electrodes deplete the charge carriers and repel the quantum Hall edge channel. The transmissions of the FP cavities are measured through the diagonal differential resistance $R_{\mathrm{D}} = \mathrm{d}V_{\mathrm{D}}/\mathrm{d}I$, where I is the current measured by an ampmeter and V_{D} the diagonal voltage drop across the contacts V_{D}^{+} and V_{D}^{-}, in voltage bias configuration using a dc and ac voltage sources, V_{dc} and V_{ac}.

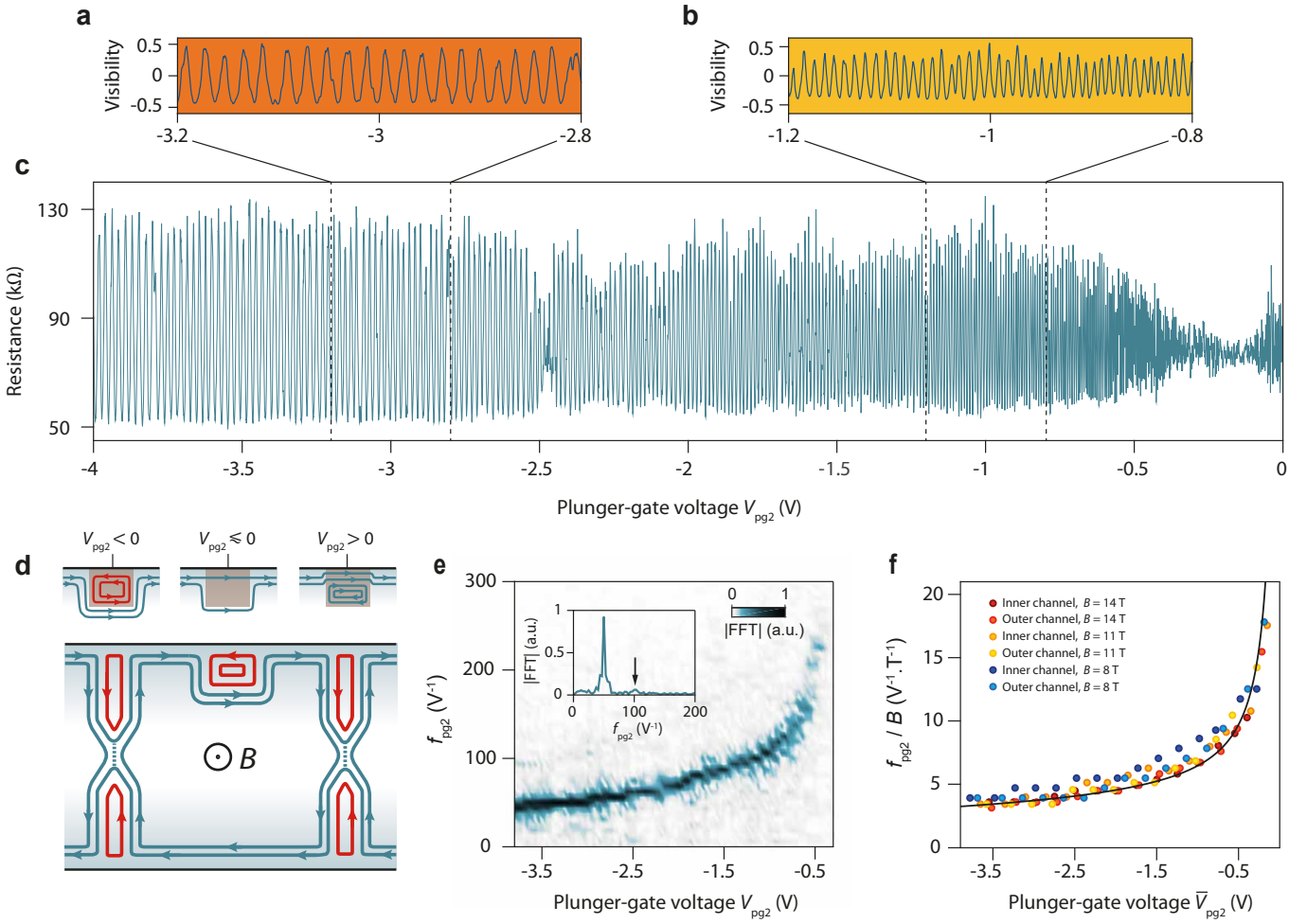

FIG. 2. **Gate-tunable quantum interference. a, b, c,** Diagonal resistance oscillations as a function of plunger-gate voltage V_{pg2} measured on the small interferometer at 0.015 K and 14 T (with an ac bias voltage of 5 μV). The back-gate voltage is set to $V_{\mathrm{bg}} = 0.533$ V corresponding to a filling factor $\nu_b = 1.5$ in the bulk. The split-gate voltages on QPC_2 and QPC_3 are tuned to obtain partial transmission of the outer edge channel. The charge neutrality point below the plunger gate is at -0.3 V and corresponds to a suppression of the oscillation amplitude in c due to the divergence of the oscillation frequency shown in e. a and b show zooms on smaller V_{pg2} ranges of the resistance oscillations converted in visibility $(R - \bar{R})/\bar{R}$, where $\bar{R}$ is the resistance average. **d,** Schematics of the QH-FP interferometer illustrating the edge channels configuration for the measurements in c. The black lines represent the physical edges of graphene. The blue (red) lines indicate electron(hole)-like edge channels and the arrows the direction of motion of charge carriers. At the QPC constriction, the dashed line indicates the tunneling of the interfering edge channel. Top sketches: Three configurations for the states around the plunger gate. Left, accumulation of localized hole states repelling the propagating electron edge channels. Middle, depletion of charge carrier density to a filling factor 1 below the gate, which repels the inner edge channel. Right, accumulation of localized electron states that push the propagating edge channels closer to the graphene edge. **e,** Fourier amplitude of the resistance oscillations in c as a function of V_{pg2} and the plunger-gate-voltage frequency f_{pg2} obtained by computing the Fourier transform over a small V_{pg2} window of 0.16 V sliding over the whole V_{pg2} range. Inset : Fourier transform at $V_{\mathrm{pg2}} = -3.28$ V showing a well-defined peak at $f_{\mathrm{pg2}} = 50$ V^{-1} and a faint peak at $f_{\mathrm{pg2}} = 100$ V^{-1} indicated by the black arrow. These peaks correspond to first order and second order (two turns in the FP loop) interference processes. **f,** Evolution of the main peak frequency f_{pg2} rescaled by the magnetic field B as a function of $\bar{V}_{\mathrm{pg2}}$, the plunger-gate voltage shifted with respect to the voltage that expels the interfering edge channel. The plot gathers a set of experiments performed with different interfering edge states and at different magnetic fields. The collapse of all data points into a single curve is fitted by an electrostatic simulation (see Supp. Section IX) of the pn-junction displacement with plunger-gate voltage (black line).

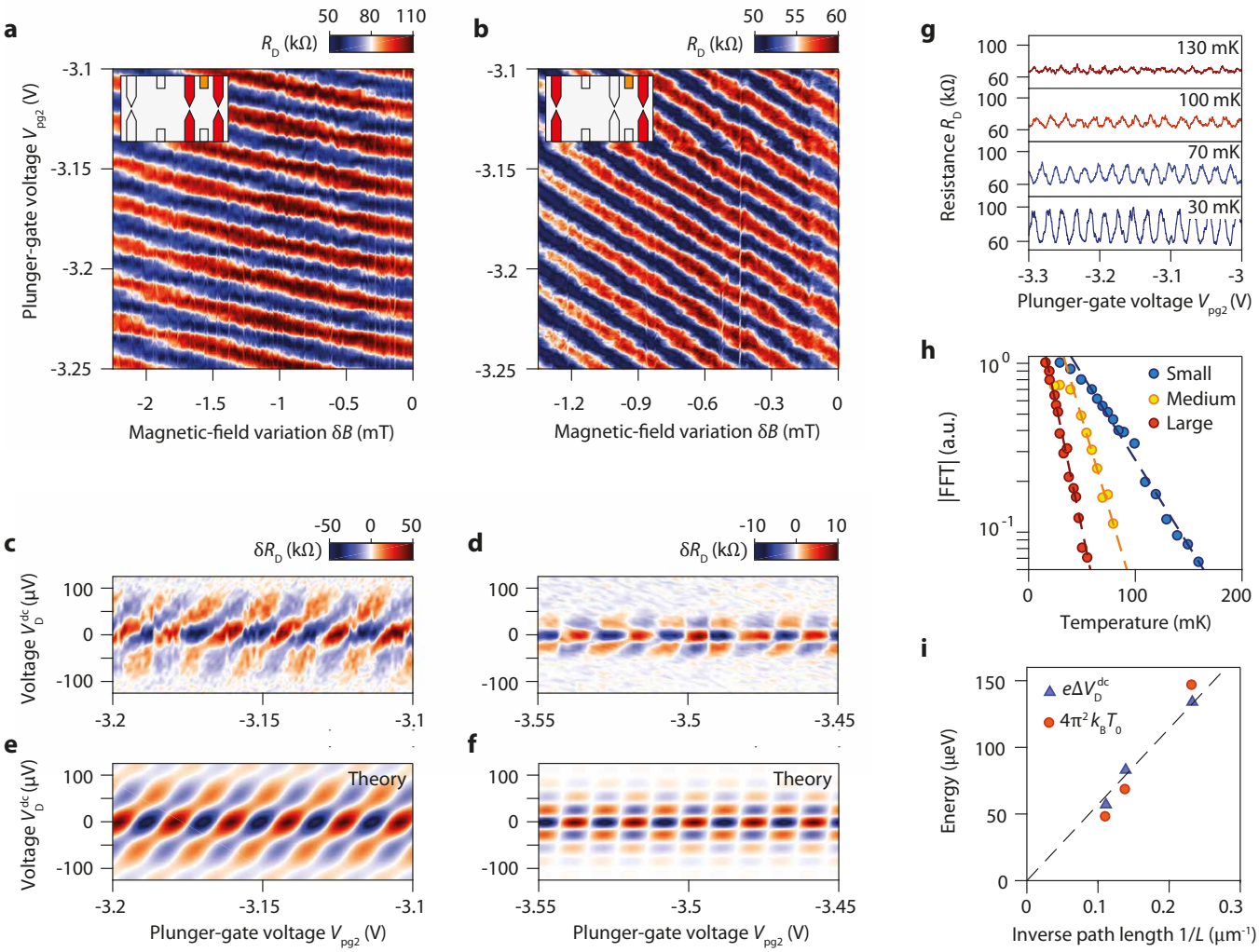

FIG. 3. **Aharonov-Bohm effect and energy dependence.** **a, b,** Diagonal resistance R_{D} versus plunger-gate voltage V_{pg2} and magnetic field variation δB measured at 0.015 K for the small interferometer in a and the large interferometer in b. The inset schematics indicate the active QPCs (in red) and plunger gates (in orange) for the respective measurements. The negative slope in the $B - V_{\mathrm{pg2}}$ plane is a clear indicator for the Aharonov-Bohm effect in both interferometers. **c, d,** Differential diagonal resistance variations δR_D, after background subtraction, versus measured dc diagonal voltage $V_{\mathrm{D}}^{\mathrm{dc}}$ and plunger-gate voltage V_{pg2} for the small interferometer in c and the large interferometer in d. Typical checkerboard patterns are observed with a significant tilt for the smallest interferometer revealing incomplete symmetrization of the voltage bias. **e, f,** Numerical simulations of resistance oscillations induced by voltage bias and plunger-gate voltage that reproduce the data presented in c and d, respectively. The simulation incorporates an asymmetric potential drop at the two QPCs and an out-of-equilibrium decoherence factor (see Supp. Section XIV). The asymmetry factor is $x = 0.2$ in e and $x = 0.02$ in f. **g,** Temperature evolution of the resistance oscillations versus plunger-gate voltage V_{pg2} for the small interferometer. **h,** Exponential decays of the Fourier amplitude of the resistance oscillations for the small (blue), medium (yellow) and large (red) interferometers. The dashed line is a fit with $\exp(-T/T_0)$ giving $T_0 = 43$, 20, and 14 mK for the small, medium, and large interferometers, respectively. **i,** Evolution of the energy scales as a function of the inverse of the cavity length L of the three interferometers. The oscillation period with the dc voltage, $\Delta V_{\mathrm{D}}^{\mathrm{dc}}$, of the checkerboard pattern corresponds to the Thouless energy E_{Th} and is expected to be equal to the energy scale $4\pi^2 k_{\mathrm{B}} T_0$ of the temperature-induced blurring of the resistance oscillations[5]. The dashed line is a linear fit highlighting the $1/L$ scaling of both energy scales. All data in this figure are obtained in a configuration with the outer edge channel interfering at $B = 14$ T.

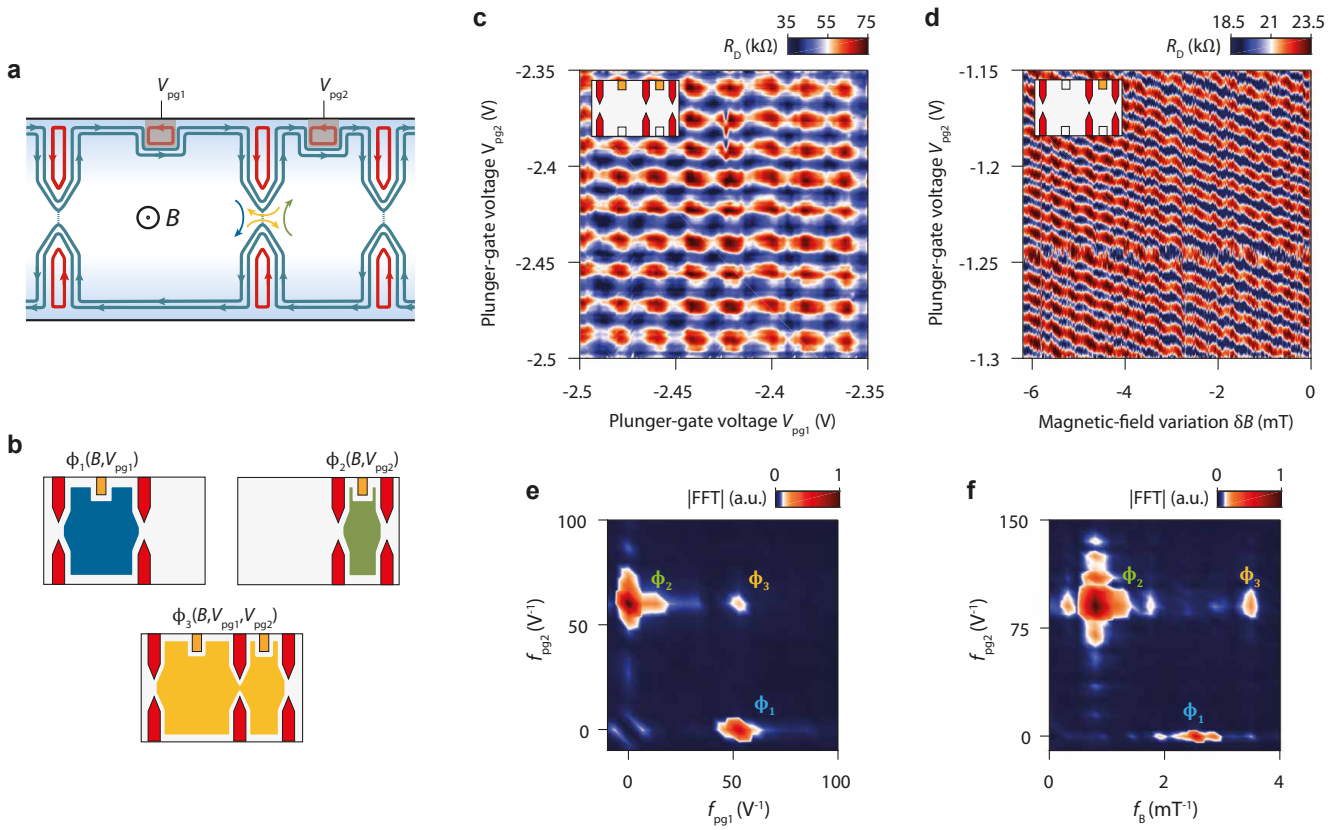

FIG. 4. **Coherently-coupled double QH-FP interferometer.** **a,** Schematics of the double QH-FP interferometer in a configuration of partial backscattering of the inner edge channel at the three QPCs. The central QPC can either reflect an incoming electron from the left cavity (blue arrow) or the right cavity (green arrow), or transmit coherently an electron from one cavity to the other (yellow arrows). In the latter case, electrons pick up the Aharonov-Bohm phase given by the combined areas of the small and medium interferometers. **b,** Schematics of the cavities involved in the different interference processes depicted in a. $\phi_{1,2,3}$ are the corresponding Aharonov-Bohm fluxes, indicated with the magnetic field and plunger-gate voltages that modulate them. **c,** Diagonal resistance versus plunger-gate voltages $V_{\rm pg1}$ and $V_{\rm pg2}$ (outer edge channel interfering, $B = 14$ T). **d,** Diagonal resistance $R_{\rm D}$ versus magnetic field variation δB and plunger-gate voltage $V_{\rm pg2}$ (inner edge channel interfering, $B = 14$ T). The inset schematics in c and d indicate the active QPCs (in red) and plunger gates (in orange) for the respective measurements. **e,** Fourier amplitude of the resistance oscillations in c versus plunger-gate-voltage frequencies $f_{\rm pg1}$ and $f_{\rm pg2}$. The three peaks at $(f_{\rm pg1}, f_{\rm pg2}) = (53\,{\rm V}^{-1}, 0\,{\rm V}^{-1})$, $(0\,{\rm V}^{-1}, 60\,{\rm V}^{-1})$ and $(53\,{\rm V}^{-1}, 60\,{\rm V}^{-1})$ correspond to the three Aharonov-Bohm fluxes depicted in b. **f,** Fourier amplitude of the resistance oscillations in d versus magnetic field frequency $f_{\rm B}$ and plunger-gate-voltage frequency $f_{\rm pg2}$. The three peaks of the three Aharonov-Bohm fluxes emerge at $(f_B, f_{\rm pg2}) = (0.79\,{\rm mT}^{-1}, 90\,{\rm V}^{-1})$, $(2.54\,{\rm mT}^{-1}, 0\,{\rm V}^{-1})$ and $(3.49\,{\rm mT}^{-1}, 90\,{\rm V}^{-1})$. In both Fourier amplitude maps, the peak that corresponds to flux $\phi_3(B, V_{\rm pg1}, V_{\rm pg2})$ reveals the quantum coherence throughout the two cavities of the double QH-FP interferometer.

Supplementary Information

I. SAMPLES STUDIED

Figure S1 displays optical images of the devices studied in this work. The fabrication process followed to fabricate these samples is described in Methods. The thickness of the van der Waals layers and the size of the split-gate gaps are reported in table I.

Sample	Top hBN thickness (nm)	Bottom hBN thickness (nm)	Graphite thickness (nm)	Split-gate gap (nm)
BNGr74	22	18	4	0 / 21 / 20
BNGr64	20	50		148 / 159
BNGr30	25	15		129 / 140

TABLE I. **Samples characteristics.** Thickness of the hBN and graphite layers measured by atomic force microscopy. Size of the gap of the split-gate electrodes measured by scanning electron microscopy.

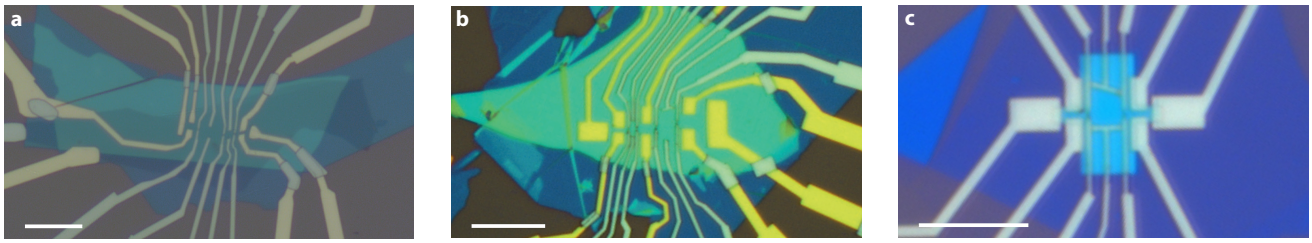

FIG. S1. **Optical images of the devices. a,** Sample BNGr74 of the main text. **b,** Sample BNGr64 described in section XII. **c,** Sample BNGr30 described in section XII. Scale bars are 10 μm.

II. PARAMETERS EXTRACTED FROM THE AHARONOV-BOHM INTERFERENCE

Table II presents the various parameters extracted from the measurements shown in Figure 3 of the main text, among which the Aharonov-Bohm period $\Delta B_{@14\,\mathrm{T}}$, the Thouless energy E_{Th} extracted from the checkerboard patterns, the energy scale T_0 related to the temperature dependence of the resistance oscillation, together with the geometrical dimensions (surfaces and lengths between QPCs) of the three Fabry-Pérot cavities.

Importantly, we stress that the determination of the device geometry relies on optical images of the graphene flake taken during the van der Waals pick up process, which makes the exact determination of the graphene edge delicate. We therefore assess the graphene edge position from this image at ± 150 nm, which results in the uncertainties of the geometrical area A_{geo} of the FP cavities and lengths L between QPCs reported in Table II.

QH-FP	$\Delta B_{@14\,\mathrm{T}}$ (mT)	A_{AB} (μm^2)	A_{geo} (μm^2)	L (μm)	E_{Th} (μV)	T_0 (mK)	$E_{\mathrm{Th}}/4\pi^2 k_{\mathrm{B}}$ (mK)
Small	1.32	3.1	3.1 ± 0.4	4.3 ± 0.5	134	43	39
Medium	0.40	10.4	10.7 ± 1.2	7.2 ± 0.5	83	20	24
Large	0.27	15.0	13.1 ± 1.8	9.0 ± 0.5	57	14	17

TABLE II. **Geometrical and physical parameters corresponding to the measurements of Fig. 3** Aharonov-Bohm period $\Delta B_{@14\,\mathrm{T}}$ obtained at $B = 14$ T and resulting Aharonov-Bohm area A_{AB}; geometrical area A_{geo} of the FP cavities; geometrical length L between two QPCs of the cavity; Thouless energy E_{Th} extracted from the checkerboard patterns in Fig. 3c and d; Energy scale T_0 extracted from Fig. 3h; $E_{\mathrm{Th}}/4\pi^2 k_{\mathrm{B}}$, the quantity theoretically equal to T_0 according to ref.[5]

III. DESIGN CHARACTERISTIC OF THE QPCS

The presence of the graphite back-gate electrode separated from the graphene by a thin hBN dielectric layer imposes drastic conditions for the design of the split-gate electrodes. Contrary to devices on Si/SiO_2 studied in ref.[41,45] in which the split-gate gap of about 150 nm led to a suitable ratio of split-gate capacitance to QPC capacitance, the very close proximity of the graphite back gate imposes a much smaller split-gate gap. By performing numerical simulations[41], we estimated the split-gate gap that leads to a ratio of split-gate capacitance to QPC capacitance of the order of 2 to be of the order of few tens of nanometers, depending on the hBN thicknesses. Figure S2 displays scanning electron micrographs of the three split gates of sample BNGr74 discussed in the main text. The split-gate gaps of QPC_2 and QPC_3 are 20 nm, suitable for operating the split gates as QPCs in the quantum Hall regime. The split-gate electrodes of QPC_1 are unintentionally connected but this short-circuit does not hinder QPC operation (see QPC characterizations in section VI).

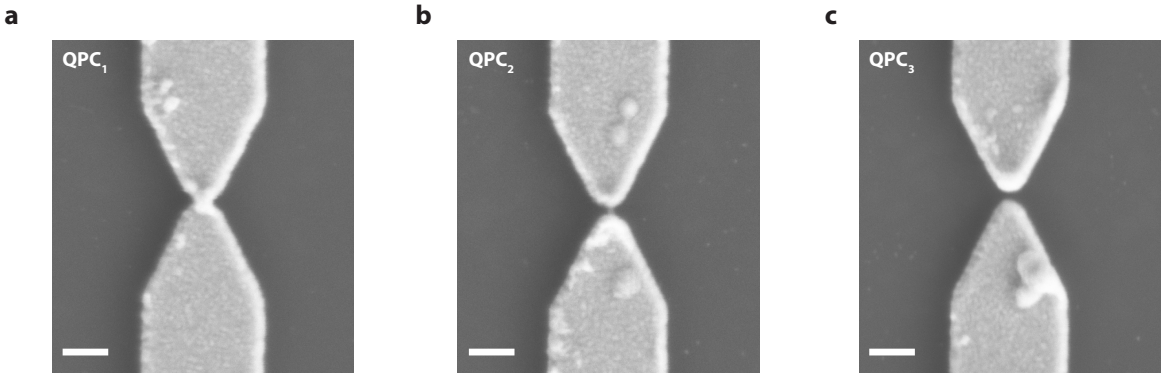

FIG. S2. **QPCs geometry.** Scanning electron micrograph of the QPCs of BNGr74 device. **a,** QPC_1. **b,** QPC_2. **c,** QPC_3. The two split-gate electrodes of QPC_1 are unintentionally connected. The gaps between the two other split gates is 20 nm. Scale bar is 100 nm.

IV. CHARACTERIZATION OF THE SPLIT-GATE CAPACITANCES AT 0 T

In this section, we present the characterization of the back gate and the different split gates at zero magnetic field for the sample of the main text. Figure S3 shows color-coded maps of the longitudinal resistance $R_{\rm xx}$ versus back-gate voltage $V_{\rm bg}$ and voltage $V_{\rm QPC}$ applied on a split gate (other split gates are floating). The maps exhibit four quadrants separated by two nearby horizontal lines and a diagonal line. The most resistive horizontal line, at $V_{\rm bg} = -0.04$ V, corresponds to the charge neutrality point in the bulk of graphene and the diagonal line corresponds to the charge neutrality point below the active split-gate electrodes, as usual for graphene devices equipped with a local top gate. The two lines intersect at $V_{\rm QPC} \simeq +0.38$ V as a result of the work function difference between the palladium of the gates and the graphene. The second horizontal line is more unusual and results from the local hole doping of the graphene beneath the two other split gates that are not active but contribute in series to the measured resistance. The palladium of these split-gate electrodes shifts the position of the charge neutrality point beneath them to $V_{\rm bg} = 0.12 - 0.18$ V, yielding a secondary resistance peak, independent of the active split gate and observed consistently for the three QPC maps. These maps also provide the capacitance ratios $C_{\rm sg}/C_{\rm bg}$ between the active split-gate and the back-gate electrodes which are respectively of 0.83 for $\rm QPC_1$ and 0.86 for $\rm QPC_2$ and $\rm QPC_3$. They are important quantities for the analysis of the QPC properties in the QH regime.

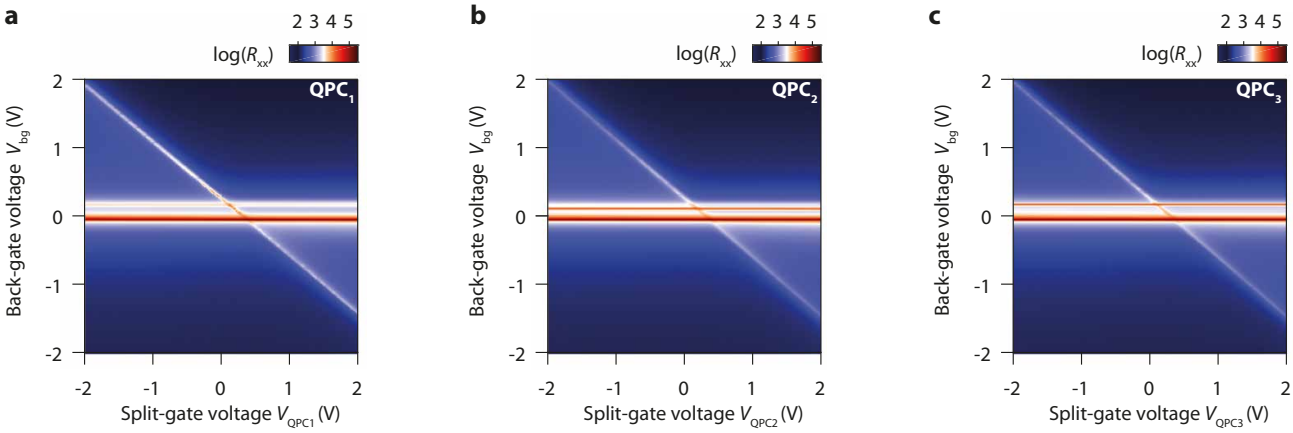

FIG. S3. **Split-gates characterization at 0 T. a, b, c,** Longitudinal resistance $R_{\rm xx}$ versus split-gate voltage $V_{\rm QPC}$ and back-gate voltage $V_{\rm bg}$ for the three QPCs of the QH-FP interferometer presented in the main text. The horizontal line at $V_{\rm bg} = -0.04$ V corresponds to the charge neutrality point in the bulk graphene, whereas the diagonal lines correspond to the charge neutrality point in the graphene beneath the active split gate. These lines intersect at $(V_{\rm QPC}, V_{\rm bg}) \simeq (+0.38\ {\rm V}, -0.04\ {\rm V})$ revealing the significant local hole doping induced by the palladium gates. The second horizontal line at $V_{\rm bg} = 0.18$ V in a and c and $V_{\rm bg} = 0.12$ V in b marks the positive back-gate voltage needed to compensate the hole doping induced by the palladium beneath the non-active split gates.

V. FAN DIAGRAM OF BULK LANDAU LEVELS

In this section, we present the Landau fan diagram of sample BNGr74. Fig. S4 displays the longitudinal resistance $R_{\rm xx}$ as a function of magnetic field B and back-gate voltage $V_{\rm bg}$, measured at 0.02 K. This measurement was performed with a voltage $V_{\rm QPC} = +0.3$ V applied on each QPC to compensate the hole doping induced by the palladium split gates and ensure a quasi-homogeneous charge carrier density in the graphene layer.

Broken-symmetry states in electron(hole)-type Landau levels emerge as minima in $R_{\rm xx}$ above 5 T (3 T), consistent with the mobility $\mu = 130\,000\,{\rm cm}^2.{\rm V}^{-1}.{\rm s}^{-1}$ obtained for a charge carrier density of $1 \times 10^{12}\,{\rm cm}^{-2}$ from Hall measurements. In addition, an insulating behaviour develops at charge neutrality with increasing magnetic field. The full-lifting of the degeneracies in the zeroth Landau level occurs above 4 T, allowing to perform interferometry experiments with the inner or outer electron edge channels of the zeroth Landau level at relatively low magnetic field values (see section XIII).

From the position of the $R_{\rm xx}$ minima, we extract a back-gate capacitance $C_{\rm bg} = 1.45$ mF/m^2 consistent with the bottom hBN thickness and a hBN dielectric constant $\epsilon_{\rm r}^{\rm BN} \approx 3$.

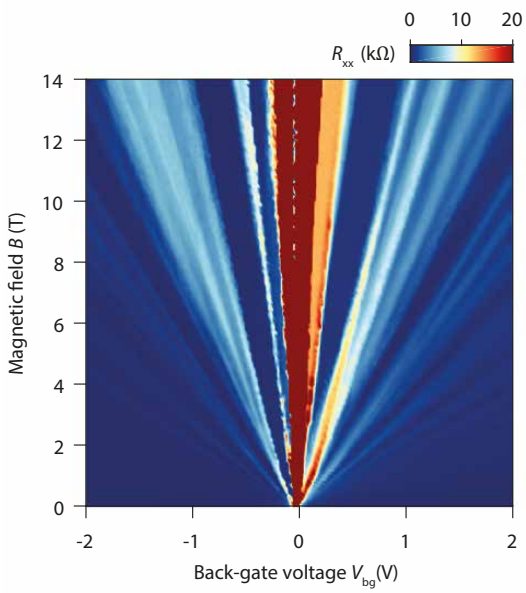

FIG. S4. **Landau fan diagram.** Longitudinal resistance $R_{\rm xx}$ of sample BNGr74 (device of the main text) versus back-gate voltage $V_{\rm bg}$ and magnetic field B, measured at 0.02 K.

VI. CHARACTERIZATION OF THE QPCS IN THE QUANTUM HALL REGIME

QH interferometry experiments require a precise knowledge of the edge-channels configuration in the bulk of graphene, beneath the split-gate electrodes and in the split-gate constrictions. This section describes the action of the split-gate electrodes in the QH regime, which allows to determine the gate-voltage set points for the (partial) QPC pinch-off and tuning of QH edge channel transmissions.

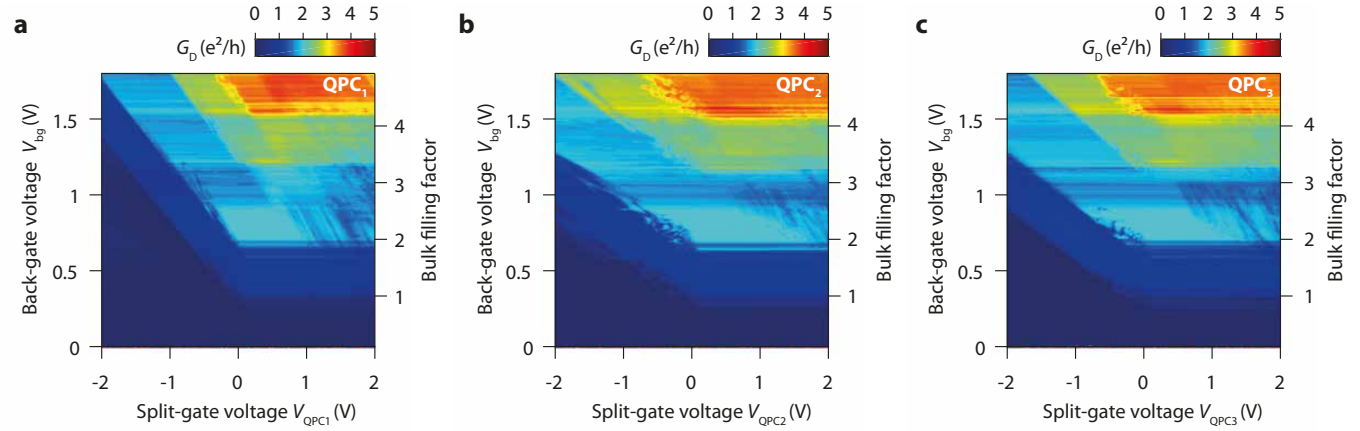

FIG. S5. **QPC conductance maps at 14 T. a, b, c,** Diagonal conductance $G_{\rm D}$ versus split-gate voltages, $V_{\rm QPC}$, and back-gate voltages, $V_{\rm bg}$, for the three QPCs of the device presented in the main text. During a measurement, only one QPC is studied and the two other sets of split gates are kept floating. The slope of the diagonal stripes corresponds to the capacitance ratio between the QPC constriction and the back gate. This slope is about twice/three times smaller than the zero-field slope for QPC_2 and QPC_3, but is only slightly smaller for QPC_1 (due to the unintentional absence of gap between the two electrodes of this QPC).

Figure S5 displays the diagonal conductance $G_{\rm D}$ as a function of split-gate and back-gate voltages, $V_{\rm QPC}$ and $V_{\rm bg}$, for the three QPCs. The three conductance maps show features similar to those reported in ref.[45] for a QPC operating in the QH regime. At negative split-gate voltages, $G_{\rm D}$ draws diagonal strips of nearly constant and quantized values. They have a smaller slope than the zero-field diagonal lines of Fig. S3, indicative of the smaller couplings at the constrictions characterized by capacitance ratios $C_{\rm QPC}/C_{\rm bg} \simeq 0.58$, 0.31 and 0.36 for QPC_1, QPC_2 and QPC_3, respectively. As demonstrated in ref.[45], the quantized $G_{\rm D}$ values indicate the number of transmitted QH edge channels through the QPC. For a given bulk filling factor, the QH edge channels can be backscattered by applying a negative split-gate voltage $V_{\rm QPC}$. For instance, at $V_{\rm bg} = 0.75$ V, the bulk filling factor is $\nu \simeq 2$, leading to the blue rhombi of $G_{\rm D} = 2e^2/h$ located near $V_{\rm QPC} = 0$ V in Fig. S5. Decreasing $V_{\rm QPC}$ to negative values, the conductance drops to the dark blue strip of $G_{\rm D} = e^2/h$, and then to $G_{\rm D} = 0$ at even more negative values. These conductance changes reflect the successive backscattering of the QH edge channels at the QPC[45]. The linecuts of Fig. S6 further illustrate such a successive pinch off of the inner and outer edge channels at $\nu \simeq 2.5$ (Fig. S6a) and the pinch off the outer edge channel at $\nu \simeq 1.5$ (Fig. S6b).

As discussed in section IV, the hole-doped graphene regions beneath the non active split-gate electrodes intervene in the transmission of the whole device when studying the properties of a particular split gate. These hole-doped regions have a lower filling factor than the bulk and can therefore backscatter some bulk QH edge channels. As a consequence, the QH plateaus as a function of back-gate voltage at $V_{\rm QPC} \sim 0$ V in the QPC maps of Fig. S5 are not centered at the integer bulk filling factors indicated on the right axis and determined by the fan diagram $R_{\rm xx}(V_{\rm bg}, B)$ at compensated split-gate voltages (see Fig. S4).

The comparison in Fig. S7 between a QPC map and the transverse Hall resistance $R_{\rm xy}$ that relates to the bulk filling factor bears out this observation. The $\nu = 2$ plateau develops at lower back-gate voltage in the Hall resistance than in the diagonal resistance across the QPCs. Despite the fact that the bulk has two QH edge channels when $1/R_{\rm xy} = \frac{2e^2}{h}$ at, for instance, $V_{\rm bg} = 0.5$ V, the non active QPCs that have lower filling factors backscatter the inner edge channel leading to $G_{\rm D} = e^2/h$ in the QPC conductance map.

Furthermore, for the data presented in the main text, we assessed the number of bulk QH edge channels through the value of the Hall resistance plateau. For all figures of the main text, we measured $1/R_{\rm xy} = \frac{2e^2}{h}$, which indicates that two edge channels propagate in the graphene bulk.

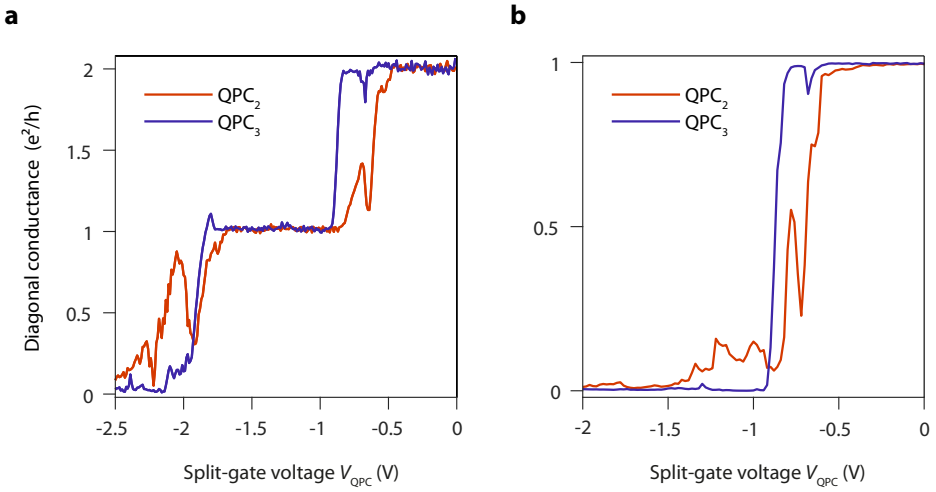

FIG. S6. **QPC transmission curves at 14 T.** Evolution of the diagonal conductance G_{D} as a function of split-gate voltages V_{QPC} at fixed back-gate voltage V_{bg}. **a,** $V_{\mathrm{bg}} = 0.88$ V. **b,** $V_{\mathrm{bg}} = 0.53$ V.

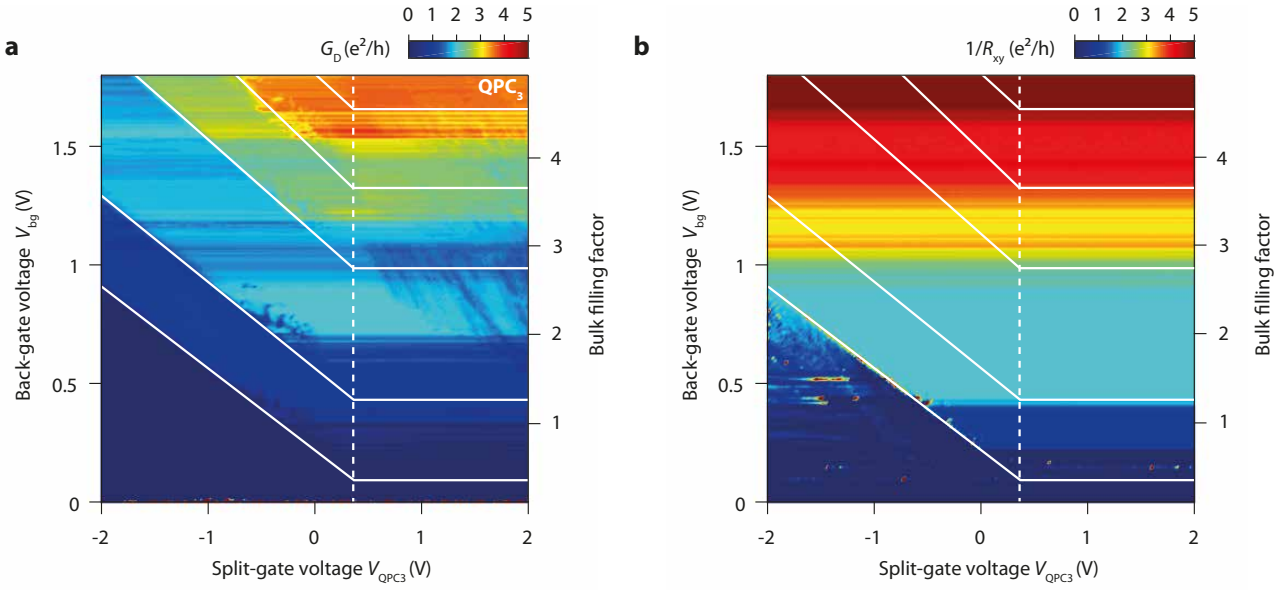

FIG. S7. **QPC map compared to Hall resistance map at 14 T. a,** Diagonal conductance G_{D} versus split-gate voltage, V_{QPC}, and back-gate voltage, V_{bg}, for QPC_3. **b,** Inverse of the transverse Hall resistance $1/R_{\mathrm{xy}}$ versus V_{QPC} and V_{bg}. The vertical dashed white line indicates the split-gate voltage that compensates the hole doping induced by the split-gate electrodes (iso-density in the bulk and beneath the active split gate). This voltage is determined in the zero-field maps of Fig. S3 at the intersection between the diagonal line and the main horizontal line of the bulk charge neutrality point. The horizontal solid white lines delineate the quantized plateaus in the Hall resistance that are centered at integer bulk filling factors (indicated on the right axis). The diagonal lines delineate the diagonal strips of constant G_{D} in the QPC map, that is, conductance plateaus given by the number of transmitted edge channels through the QPC (see ref.[45] for a detailed analysis). For consistency, these diagonal lines meet the horizontal ones of the bulk Hall resistance right at their intersect with the vertical line.

VII. AHARONOV-BOHM OSCILLATIONS AT POSITIVE PLUNGER-GATE VOLTAGE

In Fig. S8, we show the extension of the measurements performed in Fig. 2c of the main text to positive plunger-gate voltage. This corresponds to the accumulation of localized electron states beneath the plunger gate (see inset in Fig. 2c). Resistance oscillations appear clearly on the positive voltage range but with an irregular shape contrary to the oscillations at $V_{\mathrm{pg2}} < 0$ V. The Fourier amplitude of these resistance oscillations is shown in Fig. S8. The frequency of the oscillations evolves non-monotonously and is poorly defined for some voltage ranges.

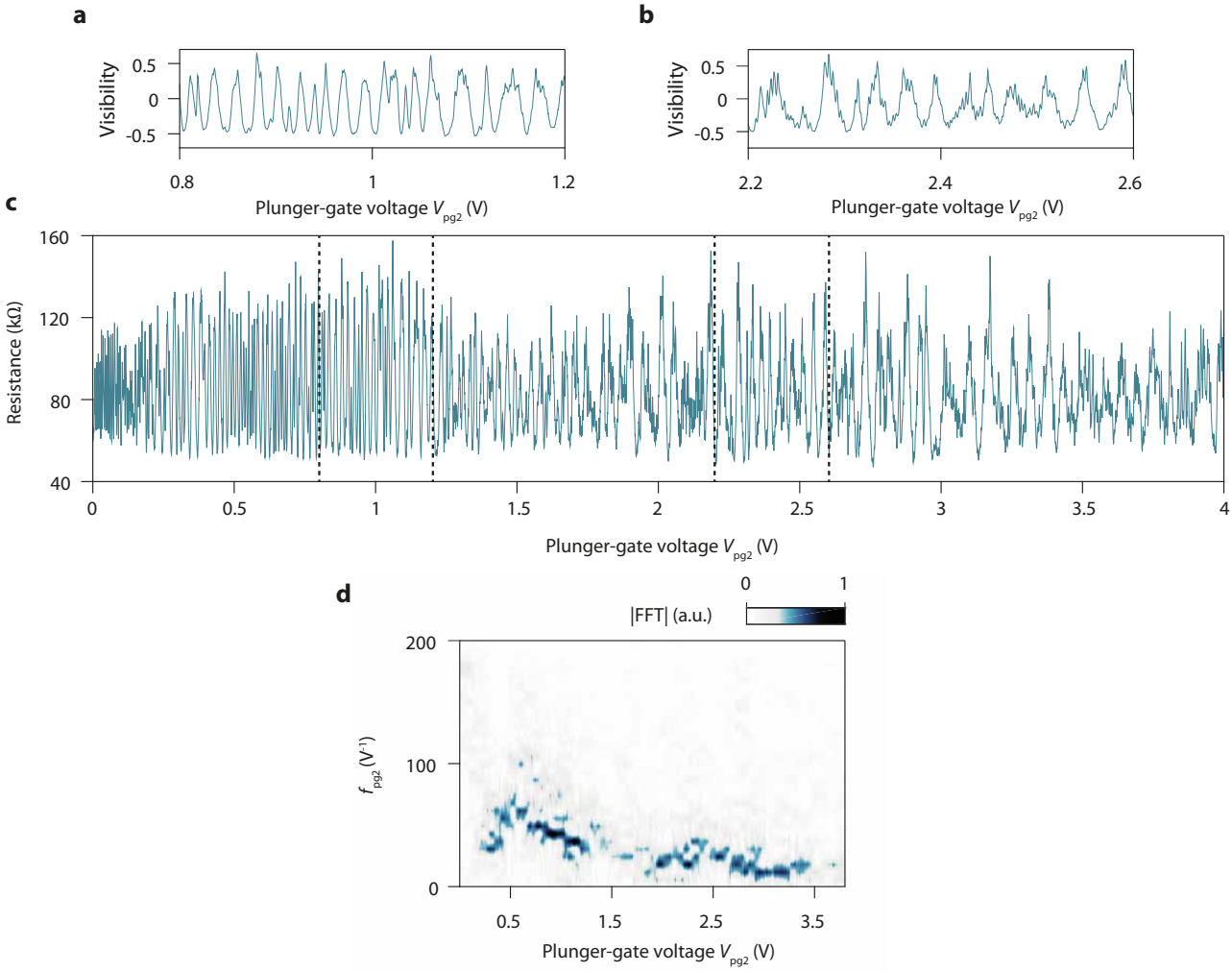

FIG. S8. **Resistance oscillations at positive plunger-gate voltage a, b, c,** Resistance oscillations as a function of plunger-gate voltage V_{pg2} measured in the small interferometer for $V_{\mathrm{pg2}} > 0$. a and b show zooms on smaller V_{pg2} ranges of the resistance oscillations converted in visibility $(R - \bar{R})/\bar{R}$, where $\bar{R}$ is the resistance background. **d,** Fourier amplitude of the resistance oscillations in c as a function of V_{pg2} and the plunger-gate voltage frequency f_{pg2}.

VIII. AHARONOV-BOHM OSCILLATIONS FOR DIFFERENT CONFIGURATIONS OF MAGNETIC FIELD AND EDGE CHANNELS

In this section we present plots of the Fourier amplitude of the resistance oscillations with V_{pg2} for experiments performed with different interfering edge channels and magnetic fields. In every cases, the frequency of the oscillations f_{pg2} is well defined and shows a clear and continuous decrease while lowering V_{pg2}. As expected for the Aharonov-Bohm regime, the frequency of the oscillations increases with the magnetic field at fixed plunger-gate voltage whereas it does not change with the interfering edge channel. A significant component oscillating at twice the Aharonov-Bohm frequency is visible on Fig. S9a. In this case, only the lowest frequency component was used to plot Fig. 2e in the main text.

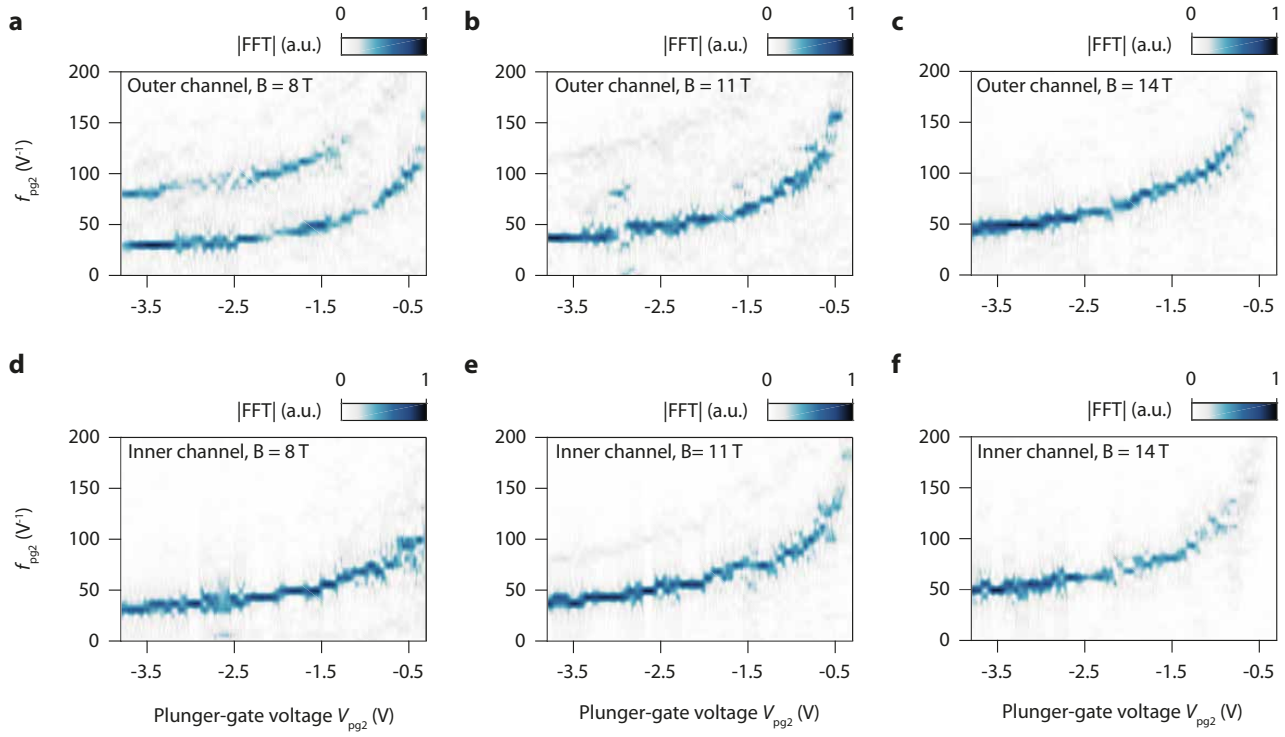

FIG. S9. **Fourier amplitude of the resistance oscillations.** Fourier amplitude of the resistance oscillations observed in the small interferometer for different configurations of magnetic field and interfering edge channel, as a function of plunger-gate voltage V_{pg2} and frequency f_{pg2}.

IX. ELECTROSTATICS OF THE PLUNGER GATE

The potential profile in the graphene below the plunger gate is determined by self-consistent electrostatic simulations in the vertical 2D plane shown in Fig. S10a assuming translational invariance in the third direction. The simulation is done for the same hBN thicknesses as in the device of the main text, with $d_{\rm bottom} = 18$ nm for the bottom layer and $d_{\rm top} = 22$ nm for the top layer. The hBN dielectric permittivity $\epsilon_{\rm r}^{\rm BN} \approx 3$ is extracted from the position of quantum Hall plateaus versus back-gate voltage. The graphite back-gate is treated as a perfect metal. The graphene sheet is modelled by a charge density $\sigma(x)$ linked to the electrostatic potential $V(x)$ by the relation :

$$\sigma(x) = (-e)\,\mathrm{sign}\big(V(x)\big)\,\frac{e^2 V(x)^2}{\pi\hbar^2 v_{\rm F}^2}$$

where $v_{\rm F} = 10^6$ m/s is the Fermi velocity in graphene. The electrostatic problem is solved self-consistently using a modified version of MaxFEM (http://www.usc.es/en/proxectos/maxfem), an electromagnetic simulation software based on the finite-element method. The mesh grid computed using Gmsh (http://gmsh.info) extends 1 μm in vertical and 2 μm in horizontal.

The self-consistent solution $V(x)$ can be calculated for a given back-gate voltage $V_{\rm bg}$ and a series of plunger-gate voltages $V_{\rm pg}$ in order to determine the dependence of the pn interface position $x_{\rm pn}$ on the plunger-gate voltage. Equivalently, the local plunger-gate capacitance $C_{\rm pg}(x)$ can be extracted from a single self-consistent simulation (for example at $V_{\rm bg} = 0$ and $V_{\rm pg} = -1$ V) using the quantum capacitance model[57]. This model is based on the relation between $\sigma(x)$ and $V(x)$ given above, together with the definition of the capacitive couplings :

$$\sigma(x) = -C_{\rm bg}\left(V_{\rm bg} - V(x)\right) - C_{\rm pg}(x)\left(V_{\rm pg} - V(x)\right)$$

where $C_{\rm bg} = \epsilon_0 \epsilon_{\rm r}^{\rm BN}/d_{\rm bottom}$. This approach based on the determination of the local capacitance $C_{\rm pg}(x)$ has the advantage to provide the self-consistent solution for any set of back-gate and plunger-gate voltages without the need to solve again the full electrostatic problem.

The spatial variation of the potential energy $E(x) = -eV(x)$ below the plunger gate is plotted in Fig. S10b for a fixed back-gate voltage $V_{\rm bg} = 0.53$ V and various negative plunger-gate voltages corresponding to the experiment reported in Fig. 2 of the main text. The position $x_{\rm pn}$ of the pn interface with respect to the gate edge is plotted in Fig. S10c as a function of the plunger-gate voltage, showing the following behavior : the formation of the pn interface occurs at $V_{\rm pg} = -0.65$ V (in the data this happens around $\simeq -0.3$ V instead, due to the hole doping of $+0.38$ V from the palladium split-gate electrodes, corresponding to the charge neutrality point below the plunger gate), then the fast displacement of the pn interface corresponds to the expulsion of the pn interface from below the plunger gate, and finally the pn interface moves slower and slower for large negative plunger-gate voltages. The displacement rate $\frac{{\rm d}x_{\rm pn}}{{\rm d}V_{\rm pg}}$ plotted in Fig. S10d is used in the main text to calculate the non-linear lever arm $\alpha = L_{\rm pg} \times \frac{{\rm d}x_{\rm pn}}{{\rm d}V_{\rm pg}}$ of the plunger gate with contour length $L_{\rm pg}$. This lever arm provides the theoretical conversion between plunger-gate voltage and interferometer area, which writes $\Delta A = \alpha\,\Delta V_{\rm pg}$, and which is compared in Fig. 2f with the oscillation frequency measured experimentally. $L_{\rm pg}$ remains an adjustable parameter because the position of the graphene edges is known with an uncertainty of ± 150 nm. To reproduce the measurement, a plunger-gate contour of $L_{\rm pg} = 1.8$ μm is used, in good agreement with the expected lithographic length of 1.5 ± 0.3 μm (the uncertainty of the graphene edge position contributes twice).

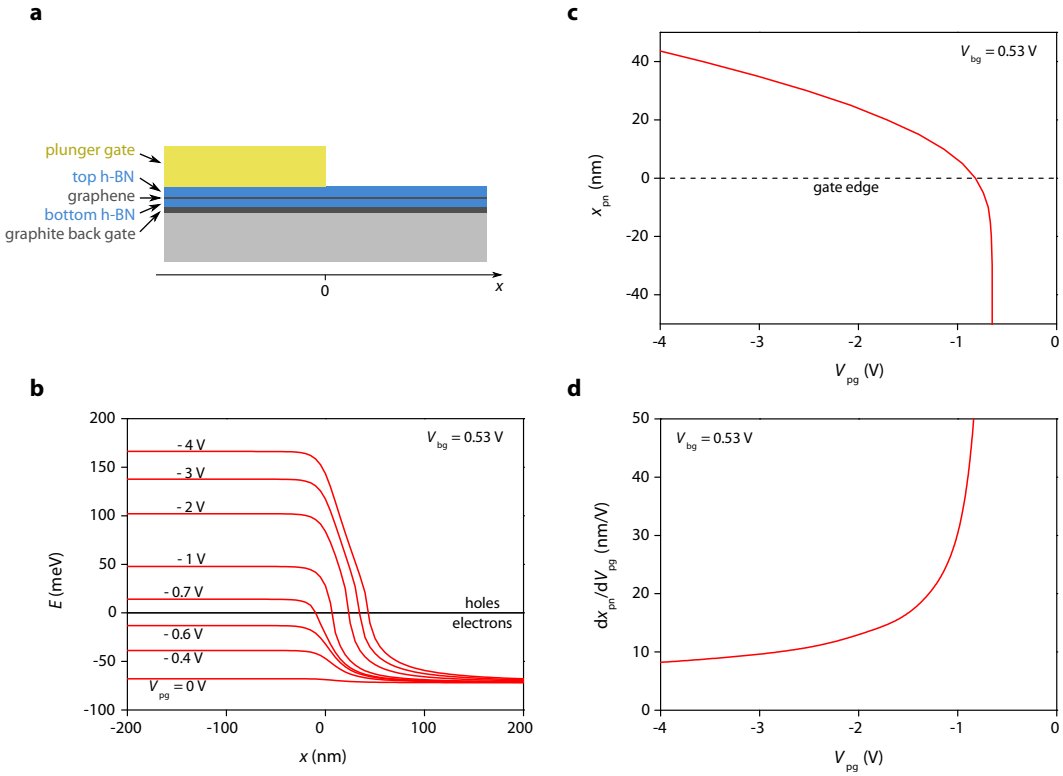

FIG. S10. **Plunger-gate electrostatics. a,** Schematics of the hBN/graphene/hBN heterostructure deposited on the graphite back gate and partially covered by the metallic plunger gate used to tune the interfering path length. **b,** Self-consistent electrostatic energy profiles $E = -eV$ in the graphene layer for a back-gate voltage $V_{\rm bg} = 0.53$ V and plunger-gate voltages $V_{\rm pg}$ varying from 0 to -4 V. **c,** Position of the pn interface with respect to the gate edge as a function of the plunger-gate voltage. **d,** Displacement rate of the pn interface calculated as its derivative with respect to the plunger-gate voltage.

X. AHARONOV-BOHM OSCILLATIONS IN THE MEDIUM INTERFEROMETER

To complement the $(\delta B, V_{\mathrm{pg}})$ maps shown in Fig. 3a and b for the small and large interferometers, we present in Fig. S11 the map obtained for the medium interferometer, in the same conditions, i.e. with the outer edge state at $B = 14$ T. The constant resistance lines have a negative slope indicating the Aharonov-Bohm origin of the oscillations. The field periodicity is 0.40 mT corresponding to an Aharonov-Bohm area of 10.4 μm^2 in good agreement with the expected lithographic area (see Table II).

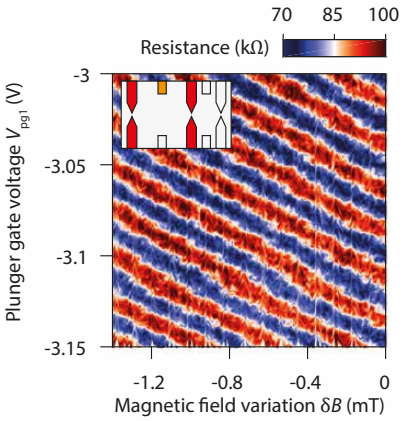

FIG. S11. **Aharonov-Bohm oscillations in the medium interferometer.** Diagonal resistance as a function of plunger-gate voltage V_{pg2} and magnetic field variation δB in the medium interferometer measured at 14 T with the outer edge channel interfering. The inset schematic indicates the active QPCs (in red) and plunger gate (in orange).

XI. INTERFEROMETRY EXPERIMENTS WITH INNER EDGE STATE AT 14 T IN THE THREE INTERFEROMETERS

In this section we present additional interferometry experiments performed with the inner edge channel of the zeroth Landau level at $B = 14$ T. Fig. S12a, b and c show the diagonal resistance of the device as a function of plunger-gate voltages and magnetic field for the small, medium and large interferometers, respectively. The results are virtually identical to those performed with the outer edge channel. The magnetic field periods extracted from these measurements are respectively of 1.23, 0.39 and 0.27 mT.

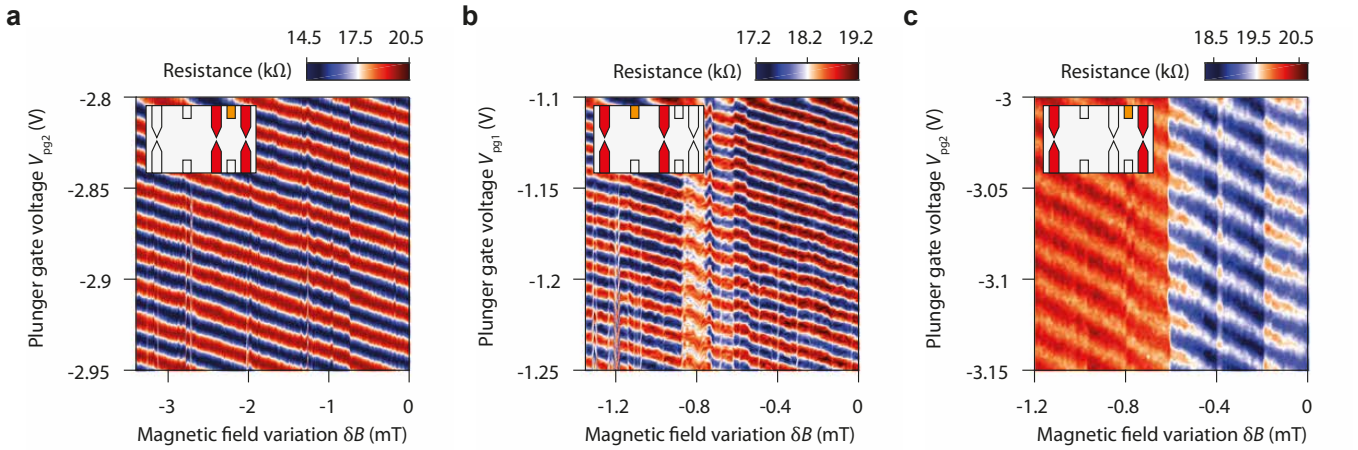

FIG. S12. **Aharonov-Bohm oscillations with the inner edge channel. a, b, c,** Diagonal resistance versus plunger-gate voltage $V_{\mathrm{pg1,2}}$ and magnetic field δB for the small, medium and large interferometers, respectively, with the inner edge channel interfering at 14 T. The inset schematics indicate the active QPCs (in red) and plunger gates (in orange).

XII. AHARONOV-BOHM OSCILLATIONS IN OTHER DEVICES

In this section we present the data obtained on two other devices, BNGr64 and BNGr30. They do not have a graphite back gate, and the silicon substrate serves as the back gate instead. Even without graphite electrode, we observed for both samples Aharonov-Bohm oscillations, indicating that the absence of charging effect is not only related to the screening by the graphite gate.

BNGr64 device

We first present the data for the device BNGr64 shown in Fig. S1b. In this device, three out of four QPCs were operating correctly enabling us to perform experiments with only one of the two interferometers, whose scanning electron micrograph is displayed in Fig. S13. This device was studied using a larger ac bias-voltage excitation of 20 μV and using the bottom plunger gate. The large plunger gate was kept grounded during the measurements.

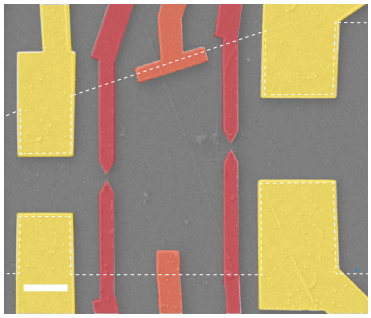

FIG. S13. **QH-FP interferometer in sample BNGr64.** False-colored scanning electron micrograph of the device. Graphene edges are represented by the white dotted line. Contacts, QPCs and plunger gates are color-coded in yellow, red and orange. Scale bar is 1 μm.

We present interferometry experiments performed with the outer interfering edge channel at 14 T with a bulk filling factor $\nu_b = 1.1$. Contrary to the data presented in the main text, there is only one electron-like edge channel propagating in the interferometer. Fig. S14c shows the evolution of the diagonal resistance with plunger-gate voltage $V_{\rm pg}$. Clear resistance oscillations are observed while decreasing $V_{\rm pg}$ from 0 to -3.2 V. Contrary to the data presented in Fig. 2c of the main text, the oscillations show many phase shifts as well as some visibility losses, reflecting the lower degree of stability and coherence of the device. The visibility of the oscillations is typically about 15% as evidenced in Fig. S14a and b. The Fourier transform amplitude of the oscillations is presented in Fig. S14d and shows a decrease of the frequency of the oscillations $f_{\rm pg}$ with the plunger-gate voltage $V_{\rm pg}$ consistent with that in Fig. 2 of the main text.

The evolution of the diagonal resistance oscillations with both the plunger-gate voltage and the magnetic field in this configuration is shown in Fig. S14e. A smooth resistance background for each sweep was subtracted to evidence lines of constant Aharonov-Bohm phase and get rid of average-conductance variations. Constant resistance values form lines with a negative slope in the δB–$V_{\rm pg}$ plane which shows that this device operates in the Aharonov-Bohm regime. From these measurements, we extract a magnetic field period of 0.42 mT corresponding to an enclosed area of 9.9 μm^2 in agreement with the geometrical surface of 11.5 μm^2.

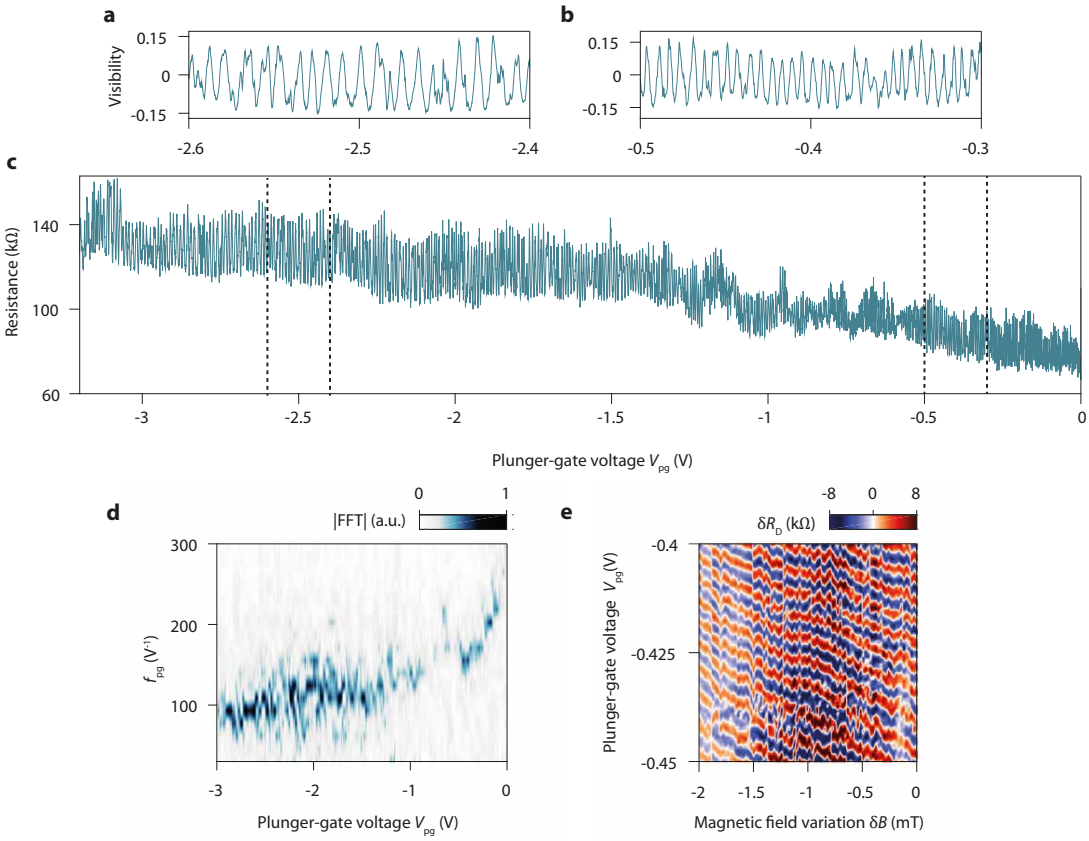

FIG. S14. **Resistance oscillations in sample BNGr64. a, b, c,** Resistance oscillations induced by change of the plunger-gate voltage $V_{\rm pg}$ in interferometry experiments with the inner edge channel at 14 T. Clear resistance oscillations are visible lowering $V_{\rm pg}$, on top of a continuous increase of the mean resistance of the device evidenced in c. a and b show zooms on smaller $V_{\rm pg2}$ ranges of the resistance oscillations converted in visibility $(R-\bar{R})/\bar{R}$, where $\bar{R}$ is the resistance background. **d,** Amplitude of the Fourier transform of resistance oscillations presented in c with respect to the plunger-gate voltage $V_{\rm pg}$ and the frequency $f_{\rm pg}$. A continuous decrease of the oscillations frequency is observed while decreasing $V_{\rm pg}$. **e,** Evolution of the resistance oscillations as function of the plunger-gate voltage $V_{\rm pg}$ and the magnetic field variation δB after subtraction of a resistance background for each plunger-gate voltage sweep. Constant $\delta R_{\rm D}$ lines have a negative slope characteristic of oscillations induced by Aharonov-Bohm effect.

BNGr30 device

Here we present the data for the device BNGr30, displayed in Fig. S1c. Contrary to the two previous samples, before the deposition of the metallic contacts and of the gates, the heterostructure was etched and shaped using a hard-mask of HSQ resist to uncover the graphene edges at determined positions. After a second e-beam lithography steps, both the contacts and the split gates were made by depositing a Cr/Au bilayer. In this device, the plunger gates cover nearly all the graphene edges between the two QPCs. A scanning electron micrograph of the device is shown in Fig. S15.

Interferometry experiments performed in this device with the inner edge channel at bulk filling factor $\nu_b = 2.3$ and 14 T are presented in Fig. S16. Resistance oscillations induced by a change of the top plunger-gate voltage $V_{\rm pg}$ are shown in Fig. S16a-c. They appear on the entire range of $V_{\rm pg}$ voltage even though the stability of the QPC is affected by the value of $V_{\rm pg}$. These oscillations have a small visibility typically varying between 2 and 5 % as shown in Fig. S16a and b. The Fourier transform analysis of the oscillations, shown in Fig. S16d reveals a similar lowering of the frequency $f_{\rm pg}$ of the oscillations with the plunger-gate voltage (the absence of well-defined frequency for the oscillations at $V_{\rm pg} \simeq -1.2$ V arises from the rapid drop of the resistance background).

In Fig. S16e, we show the evolution of resistance oscillations with both the magnetic field and the plunger-gate voltage. The constant phase lines have a negative slope evidencing that the oscillations result from the Aharonov-Bohm effect. We can extract a magnetic field period of 0.37 mT corresponding to an area enclosed by the interfering edge state of 11.2 μm^2 in good agreement with geometric area of 10.1 μm^2.

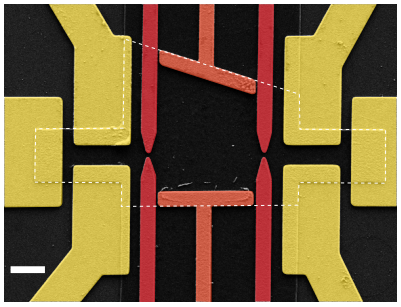

FIG. S15. **QH-FP interferometer in sample BNGr30.** False-colored scanning electron micrograph of the device. Graphene edges are represented by the white dotted line. Contacts, QPCs and plunger gates are color-coded in yellow, red and orange, respectively. Scale bar is 1 μm.

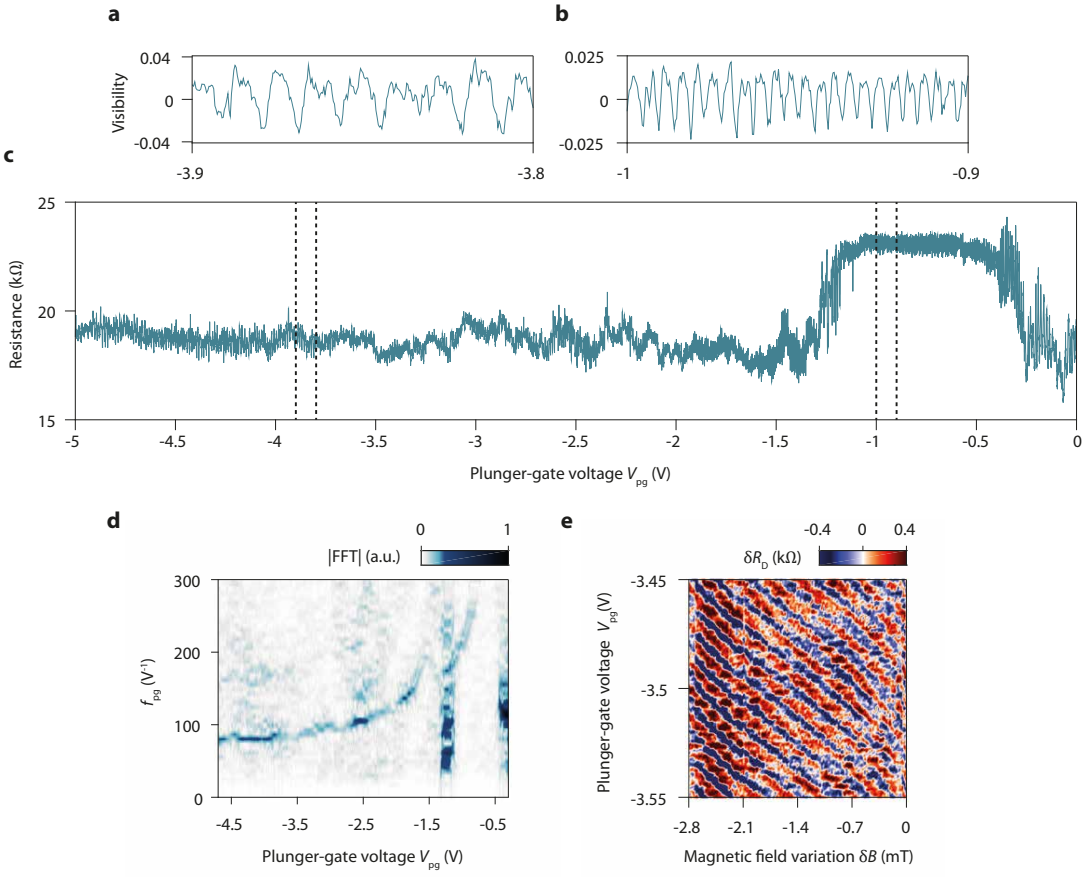

FIG. S16. **Resistance oscillations in sample BNGr30. a, b, c,** Resistance oscillations induced by a change of the plunger-gate voltage $V_{\rm pg}$ in interferometry experiments with the inner edge state at 14 T. The abrupt change in c of the mean resistance value at $V_{\rm pg} \approx -1.2$ V and $V_{\rm pg} \approx -0.2$ V might originate from instability of the QPCs. a and b show zooms on smaller $V_{\rm pg}$ ranges of the resistance oscillations converted in visibility $(R - \bar{R})/\bar{R}$, where $\bar{R}$ is the resistance background. **d,** Amplitude of the Fourier transform of resistance oscillations presented in c with respect to the plunger-gate voltage $V_{\rm pg}$ and the corresponding voltage frequency $f_{\rm pg}$. A continuous decrease of the oscillations frequency is observed while decreasing $V_{\rm pg}$. The divergence at $V_{\rm pg} \approx -1.2$ V is an artefact arising from the rapid change of the mean resistance value at this plunger-gate voltage. **e,** Evolution of the resistance oscillations with both the plunger-gate voltage $V_{\rm pg}$ and the magnetic field variation δB after subtraction of a resistance background for each plunger-gate voltage sweep. Constant $\delta R_{\rm D}$ lines have a negative slope characteristic of oscillations induced by the Aharonov-Bohm effect.

Absence of charging effects

Finally, we discuss the absence of Coulomb blockade in these devices. We emphasize that, contrary to the sample of the main text, these two devices are not equipped with a graphite gate that can considerably screen the long range Coulomb interaction and reduce the charging energy of the FP cavity. We conjecture that the large accumulation of hole states beneath the split gates may contribute to the screening of the charging energy of the FP cavity, by capacitive coupling to either the source and drain or to the split-gate electrodes that are only at few tens of nanometers above the graphene. This makes graphene an intrinsically screened 2DEG which is extremely interesting for further investigations in the fractional quantum Hall regime.

XIII. INTERFERENCES AT LOWER MAGNETIC FIELDS

Here we show that the device BNGr74 presented in the main text can also operate at low magnetic field. Stable Aharonov-Bohm interference were observed with the outer and inner edge channels respectively down to 5 T and 4 T as displayed in Fig. S17a and b. The respective Fourier amplitudes of the resistance oscillations are shown in Fig. S17c and d.

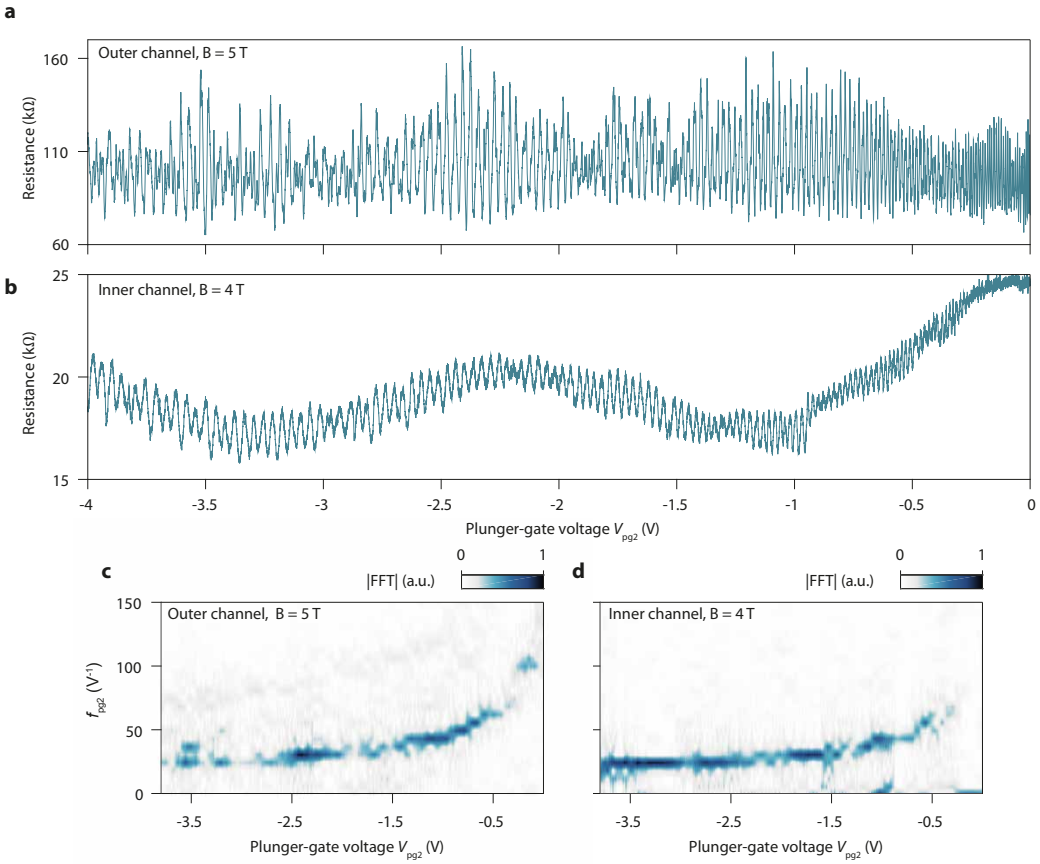

FIG. S17. **Resistance oscillations at low magnetic fields. a, b,** Resistance oscillations as a function of plunger-gate voltage V_{pg2} measured in the small interferometer at 5 T with the outer edge channel, and 4 T with the inner edge channel, respectively. **c, d,** Fourier amplitude of the resistance oscillations in a and b.

XIV. AHARONOV-BOHM OSCILLATIONS VERSUS DC VOLTAGE BIAS : ASYMMETRY AND DECAY

In this section, we discuss the oscillations induced by the application of a dc voltage bias and explain the origin of the asymmetric checkerboard pattern. We also analyze the decay of the oscillations amplitude with the voltage bias related to an energy relaxation process.

Theoretical model describing the effect of asymmetric biasing

Here, we derive the formula for the transmission of a QH-FP interferometer as a function of magnetic field and voltage bias using the same formalism as in ref.[5], but we take into account a possible asymmetric potential drop at the two beam-splitters.

The transmission of a non-interacting QH Fabry-Pérot interferometer reads:

$$t(\epsilon,\Phi) = \frac{t_1 t_2 e^{i\pi\frac{\Phi}{\Phi_0}+i\frac{L\epsilon}{\hbar v}}}{1-r_1^{'}r_2 e^{2i\pi\frac{\Phi}{\Phi_0}+i\frac{2L\epsilon}{\hbar v}}}, \tag{1}$$

where $2\pi\frac{\Phi}{\Phi_0}$ is the Aharonov-Bohm phase, $\frac{2L\epsilon}{\hbar v}$ the dynamical phase accumulated by electrons after one winding in the cavity, t_1 and t_2 the transmission amplitudes of QPC_1 and QPC_2 for right moving particles, r_1' the reflection amplitude for left-movers at QPC_1 and r_2 the reflection amplitude for right-movers at QPC_2.

The transmission probability is :

$$T(\epsilon,\Phi) = \frac{\mid t_1 \mid^2 \mid t_2 \mid^2}{1+\mid r_1^{'}r_2 \mid^2 -2 \mid r_1^{'}r_2 \mid \cos(2\pi\frac{\Phi}{\Phi_0}+\frac{2L\epsilon}{\hbar v}+\varphi)}, \tag{2}$$

where φ is a constant phase factor. Given that $\mid r_{1,2} \mid^2 = \mid r'_{1,2} \mid^2 = R_{1,2}$ and $\mid t_{1,2} \mid^2 = T_{1,2}$, we can rewrite (2) as

$$T(\epsilon,\Phi) = \frac{T_1 T_2}{1+R_1R_2-2\sqrt{R_1R_2}\cos(2\pi\frac{\Phi}{\Phi_0}+\frac{2L\epsilon}{\hbar v}+\varphi)}. \tag{3}$$

In the weak backscattering limit, $R_i \ll 1$, and omitting the phase term φ, we obtain at first order :

$$T(\epsilon,\Phi) = 1-R_1-R_2+2\sqrt{R_1R_2}\cos\left(2\pi\frac{\Phi}{\Phi_0}+\frac{2L\epsilon}{\hbar v}\right) \tag{4}$$

We then consider a finite dc voltage bias V applied between source and drain contacts. We note $q=-e<0$ the electron charge. Depending on the energy relaxation processes consecutive to the current flow, and on the electrostatic coupling between the cavity, the back gate and the source and drain, the electrochemical potential in the cavity will adjust itself at a value intermediate between that of the source and that of the drain. The right-movers coming from the source contact have an energy $qV^+ = qV(\frac{1}{2}+x) = qV\beta$ with respect to the chemical potential within FP cavity and the left-movers coming from the drain have an energy $qV^- = -qV(\frac{1}{2}-x) = -qV\overline{\beta}$. In these expressions, $x \in [-\frac{1}{2},\frac{1}{2}]$ is the voltage bias asymmetry factor. $x=0$ corresponds to a symmetric biasing with $V^+ = \frac{V}{2}$ and $V^- = -\frac{V}{2}$, meaning that the potential drop is the same across both QPCs. When $x=\frac{1}{2}$ (or equivalently $x=-\frac{1}{2}$) the bias is completely asymmetric, $V^+=V$ and $V^-=0$ (or equivalently $V^+=0$ and $V^-=-V$), the potential drop only occurs at one QPC while the FP cavity is at the same potential as one of the two contacts.

At zero temperature, the total current through the device is given by $I=\frac{q}{h}\int_{qV^-}^{qV^+} T(\epsilon,\Phi)\mathrm{d}\epsilon$:

$$I = \frac{q}{h}\int_{qV^-}^{qV^+}\left[1-R_1-R_2+2\sqrt{R_1R_2}\cos\left(2\pi\frac{\Phi}{\Phi_0}+\frac{2L\epsilon}{\hbar v}\right)\right]d\epsilon = I_0 + I_{\mathrm{osc}}, \tag{5}$$

where $I_0 = \frac{e^2}{h}(1-R_1-R_2)V$ is the constant part of the current and I_{osc} is the oscillating part of the current which writes:

$$I_{\mathrm{osc}} = 2\frac{e^2}{h}\sqrt{R_1R_2}\frac{\hbar v}{2Lq}\left[\sin\left(2\pi\frac{\Phi}{\Phi_0}+\frac{2L}{\hbar v}qV\beta\right)-\sin\left(2\pi\frac{\Phi}{\Phi_0}-\frac{2L}{\hbar v}qV\overline{\beta}\right)\right]. \tag{6}$$

The corresponding differential conductance is then :

$$\frac{dI_{\rm osc}}{dV} = g_{\rm osc}\left[\beta\cos\left(2\pi\frac{\Phi}{\Phi_0} - \frac{2L}{\hbar v}eV\beta\right) + \overline{\beta}\cos\left(2\pi\frac{\Phi}{\Phi_0} + \frac{2L}{\hbar v}eV\overline{\beta}\right)\right], \tag{7}$$

with $g_{\rm osc} = 2\frac{e^2}{h}\sqrt{R_1R_2}$ and restoring $q = -e$.

When the potential drop is symmetrical, that is, $V^+ = V/2$ and $V^- = -V/2$, we have $\beta = \overline{\beta} = \frac{1}{2}$ ($x = 0$) and then :

$$\frac{dI_{\rm osc}}{dV} = g_{\rm osc}\cos\left(2\pi\frac{\Phi}{\Phi_0}\right)\cos\left(2\pi\frac{L}{hv}eV\right), \tag{8}$$

leading to a checkerboard pattern.

If the bias is completely asymmetrical, for example when $V^+ = V$ and $V^- = 0$ with $\beta = 1$ and $\overline{\beta} = 0$ ($x = \frac{1}{2}$), we obtain

$$\frac{dI_{\rm osc}}{dV} = g_{\rm osc}\cos\left(2\pi\frac{\Phi}{\Phi_0} - 2\pi\frac{2L}{hv}eV\right) \tag{9}$$

that draws a diagonal strip pattern. Any intermediate value of x leads to a mixed pattern, that is, a tilted checkerboard as shown in Fig. 3e of the main text. Note that the diagonal resistance $\delta R_{\rm D} = -\frac{{\rm d}I_{\rm osc}}{{\rm d}V}(\frac{h}{e^2})^2$ shows exactly the same oscillatory features as the conductance in the weak backscattering limit.

In our experiment, we apply a dc voltage to the source contact while the drain contact is kept grounded. The electrostatic coupling of the cavity to the back-gate electrode results in an asymmetric potential drop which could explain why the checkerboard patterns of our two smallest interferometers are tilted. On the other hand, the fact that the checkerboard pattern is nearly symmetric for the largest interferometer, indicates that energy relaxation processes equilibrate the chemical potential for sufficiently large interferometers, leading to a symmetric potential drop. Interestingly, tilted checkerboards in QH-FP interferometers has never been reported for GaAs QH-FP devices of the same size as our small interferometer, possibly due to the larger back-gate coupling in our graphene device equipped with a graphite back gate, or because the chemical potential equilibration is less effective in graphene.

In Fig. S18, we gather the results obtained in the three different interferometers as a function of voltage bias (Fig. S18a, c, d and f are respectively identical to Fig. 3c, d, e and f). The checkerboard patterns are tilted for our small (a) and medium interferometers (b), whereas the tilt is hardly visible for the largest interferometer (c). Using eq. (7), we can quantitatively reproduce in Fig. S18d, e and f the three experimental checkerboards with asymmetry parameters $x = 0.2$, 0.1 and 0.02, respectively.

Energy relaxation

For an asymmetric potential drop characterized by an asymmetry factor x, the amplitude of the flux-periodic oscillations given by eq. 7 oscillates versus bias voltage with the following dependence :

$$\mathcal{A}\left(V, E_{\rm Th}/e\right) = \sqrt{\cos^2\left(2\pi\frac{eV}{E_{\rm Th}}\right) + 4x^2\sin^2\left(2\pi\frac{eV}{E_{\rm Th}}\right)} \tag{10}$$

In Fig. S18a, b and c, however, we observe that the oscillations amplitude decays rapidly with the bias voltage and vanishes typically after one voltage period. Such a fast decay is much faster than the $1/\Delta V$ dependence predicted in ref.[5] and was already reported by McClure and coworkers[14] in GaAs QH-FP interferometers. These authors found that an exponential decay of the oscillations amplitude with the bias describes correctly the data. Theoretical investigations[24] confirmed that Coulomb interactions can lead to an approximate exponential decay. Following this approach, we fitted the oscillations in our data with :

$$\mathcal{A}(V, \Delta V_{\rm exp})\exp\left(-2\pi\chi\frac{|V|}{\Delta V_{\rm exp}}\right), \tag{11}$$

where χ is a phenomenological parameter that describes how fast the oscillations vanish with voltage, and $\Delta V_{\rm exp}$ is the period of the resistance oscillations for this exponential decay. The amplitude of the oscillations is obtained

by computing the Fourier amplitude of the resistance oscillations as a function of the plunger-gate voltage at fixed bias voltage. This leads to the lobe structure shown in Fig. S18g, h and i. A good agreement between the model and the data is found for the three interferometers. The extracted voltage periods $\Delta V_{\rm exp}$ and damping factors χ are reported in Table III. It is worth noticing, however, that this phenomenological model does not capture the absence of secondary lobes in the experiments, suggesting that the decay of the oscillations is faster than exponential.

We therefore consider a second model with a Gaussian decay of the bias-induced oscillations. Investigations in Mach-Zehnder interferometers revealed that a Gaussian decay may arise from phase fluctuations of the interfering edge channel due to Coulomb interactions or the electric noise in the non-interfering edge channels[47,58–60]. Within this approach, we fitted our data with :

$$\mathcal{A}(V, \Delta V_{\rm gauss}) \exp\left(-\frac{V^2}{2{V_0}^2}\right), \tag{12}$$

where V_0 is the voltage scale characterizing the width of the Gaussian envelope, and $\Delta V_{\rm gauss}$ the period of the resistance oscillation for this Gaussian decay. The fits of the experimental data with this expression are displayed in Fig. S18g, h and i (orange lines). This second model also describes well the data. The extracted voltage periods $\Delta V_{\rm gauss}$, reported in Table III, are close to those obtained with the exponential decay model. The extracted V_0 values scale linearly with the inverse interfering path length $1/L$ as mentioned in ref.[47] and is typically one third of $\Delta V_{\rm gauss}$.

The qualitative difference between the exponential and Gaussian decays is that the exponential decay fits better the amplitude of the first lobe but fails to reproduce the vanishing of the second ones, whereas the Gaussian model is less accurate for the first lobe but shows a suppressed second lobe.

QH-FP	$\Delta V_{\rm exp}$ (μV)	χ	$\Delta V_{\rm gauss}$ (μV)	V_0 (μV)
Small	134	0.42	128	40
Medium	83	0.42	81	25
Large	57	0.35	61	21

TABLE III. **Fitting parameters for the different models of bias-induced oscillation decay.** Voltage period $\Delta V_{\rm exp}$ for the exponential decay model; χ damping rate for the exponential decay model; voltage period $\Delta V_{\rm gauss}$ for the Gaussian decay model; V_0 width of the Gaussian envelope.

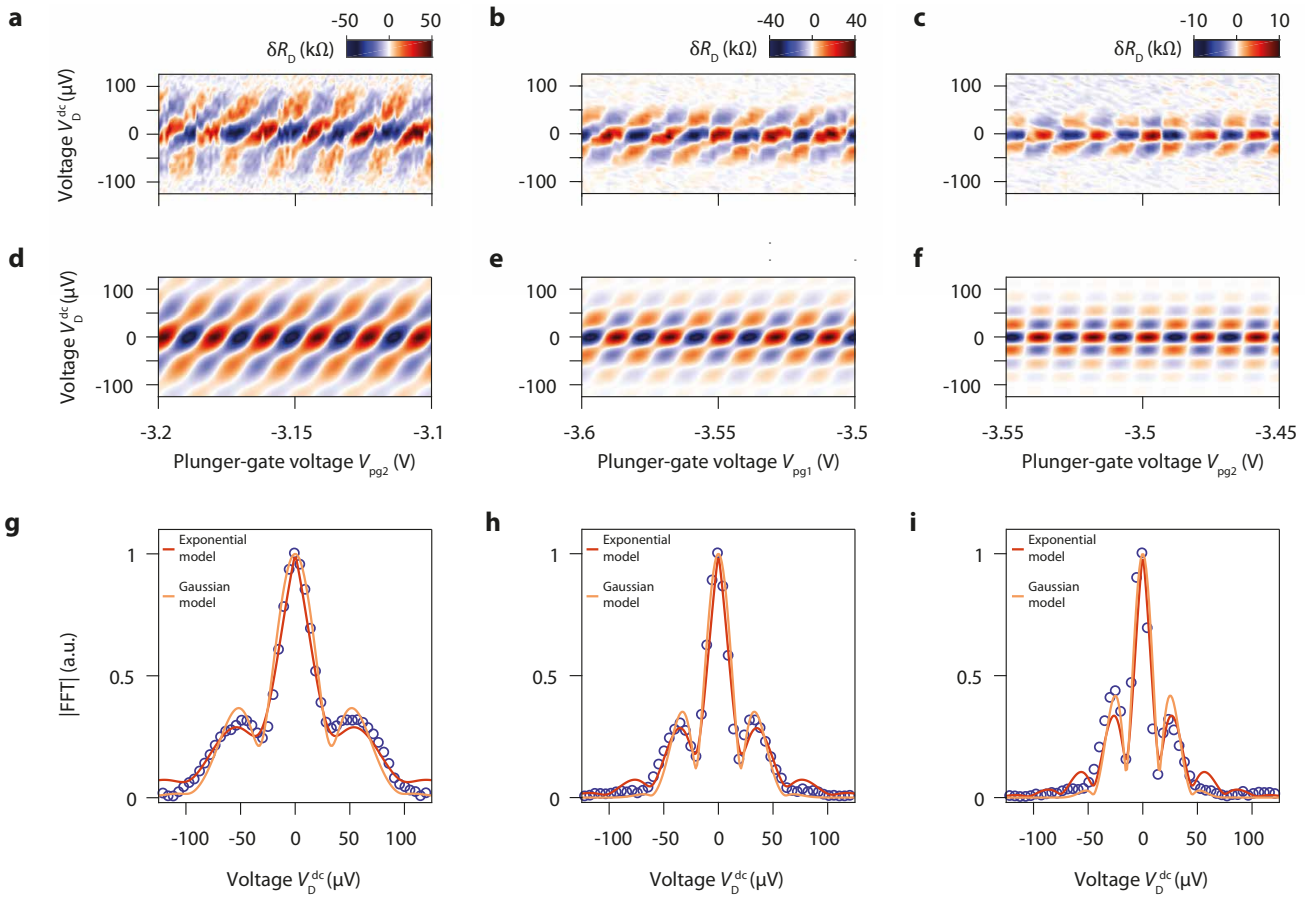

FIG. S18. **Bias dependence of Aharonov-Bohm oscillations. a, b, c,** Differential diagonal resistance variations δR_D, after background subtraction, versus dc diagonal voltage $V_{\mathrm{D}}^{\mathrm{dc}}$ and plunger-gate voltage $V_{\mathrm{pg1,2}}$ for the small, medium and large interferometer respectively in a, b and c. Interferences are obtained with the outer edge channel at 14 T. **e, f, g,** Numerical simulations of resistance oscillations induced by voltage bias and plunger-gate voltage that reproduce the data presented in a, b and c, respectively. The simulations incorporate an asymmetric potential drop at the two QPCs and an out-of-equilibrium decoherence factor. The voltage bias asymmetry factors of $x = 0.2$ and $x = 0.1$, respectively for the small d and medium interferometer e, are significant, indicating a limited chemical potential equilibration as opposed to the large interferometer f, which has a very small asymmetry term $x = 0.02$. **g, h, i,** Amplitude of the Fourier transform of the oscillations at fixed voltage bias (blue dots) and fits with eq. (11) (red line) and eq. (12) (orange line). Fitting parameters are reported in Table III.

XV. TEMPERATURE DEPENDENCE OF THE AHARONOV-BOHM OSCILLATIONS: THERMAL AVERAGING

The effect of temperature on the visibility of the Aharonov-Bohm oscillations has been calculated in ref.[5] in the limit of weak backscattering and at finite bias voltage with a symmetric potential drop at the two constrictions. Here we give the details of the calculations and extend the result to an asymmetric potential drop. Note that these calculations only consider the thermal averaging of the interference and do not introduce decoherence by inelastic scattering or energy relaxation at finite bias.

Using the notations of ref.[5], we define the tunneling amplitudes Γ_i which are responsible for the backscattering from one sample edge to the opposite sample edge at the constrictions $i = 1$ and 2. In presence of a magnetic flux Φ in the interferometer, the tunneling amplitudes can be written as $\Gamma_{1,2} = |\Gamma_{1,2}|e^{\mp i\pi\Phi/\Phi_0}$ where $\Phi_0 = h/e$ is the magnetic flux quantum. The reflection amplitudes r_i of the two mirrors forming the Fabry-Perot interferometer are given by :

$$r_i = \frac{-i2\pi\Gamma_i^*}{1+\pi^2|\Gamma_i|^2} \tag{13}$$

The transmission amplitude of the interferometer at an energy E above the Fermi level writes :

$$t(E,\Phi) = \frac{t_1 t_2}{1 + r_1 r_2^* e^{iE2L/\hbar v}} \tag{14}$$

where L is the distance between the two constrictions and v is the edge-state velocity. Note that the magnetic flux dependence is hidden in the phase of the reflection amplitudes. The transmission coefficient then writes :

$$T(E,\Phi) = \frac{|t_1|^2|t_2|^2}{1 + |r_1|^2|r_2|^2 + r_1 r_2^* e^{iE2L/\hbar v} + r_1^* r_2 e^{-iE2L/\hbar v}} \tag{15}$$

In the limit of weak back-scattering at the constrictions with $|\Gamma_i| \ll 1$, the transmission coefficient can be simplified and writes :

$$T(E,\Phi) = 1 - 4\pi^2\left(|\Gamma_1|^2 + |\Gamma_2|^2 + \Gamma_1^*\Gamma_2 e^{iE2L/\hbar v} + \Gamma_1\Gamma_2^* e^{-iE2L/\hbar v}\right) \tag{16}$$

Symmetric potential drop

Assuming a symmetric potential drop at the two constrictions as in ref.[5], the current at finite temperature T and finite voltage V is given by :

$$I(\Phi,V,T) = \frac{q}{h}\int_{-\infty}^{+\infty} T(E,\Phi)\left(\frac{1}{1+e^{(E-\frac{qV}{2})/k_\mathrm{B}T}} - \frac{1}{1+e^{(E+\frac{qV}{2})/k_\mathrm{B}T}}\right)\mathrm{d}E, \tag{17}$$

where $q < 0$ is the electron charge. Using the expression of the transmission coefficient in the limit of weak back-scattering, the current writes :

$$I(\Phi,V,T) = \frac{q^2}{h}(1-R_1-R_2)V - \frac{q}{h}\sqrt{R_1R_2}\left(e^{i2\pi\Phi/\Phi_0}H(V,T) + e^{-i2\pi\Phi/\Phi_0}H(V,T)^*\right), \tag{18}$$

where we introduce the function :

$$H(V,T) = \int_{-\infty}^{+\infty} e^{iE2L/\hbar v}\left(\frac{1}{1+e^{(E-\frac{qV}{2})/k_\mathrm{B}T}} - \frac{1}{1+e^{(E+\frac{qV}{2})/k_\mathrm{B}T}}\right)\mathrm{d}E. \tag{19}$$

By changing the variable in the integral, it becomes :

$$H(V,T) = \left(e^{i\frac{qV}{2}2L/\hbar v} - e^{-i\frac{qV}{2}2L/\hbar v}\right)\int_{-\infty}^{+\infty} e^{iE2L/\hbar v}\,\frac{1}{1+e^{E/k_\mathrm{B}T}}\,\mathrm{d}E, \tag{20}$$

where the choice of a symmetric potential drop influences only the term in the parenthesis. The calculation of the integral gives:

$$\int_{-\infty}^{+\infty} e^{iE2L/\hbar v}\,\frac{1}{1+e^{E/k_{\mathrm{B}}T}}\,\mathrm{d}E = -i2\pi k_{\mathrm{B}}T\sum_{n=0}^{+\infty} e^{-\omega_n 2L/\hbar v} = \frac{-i2\pi k_{\mathrm{B}}T}{2\sinh(\pi k_{\mathrm{B}}T2L/\hbar v)}, \tag{21}$$

where $\omega_n = (2n+1)\pi k_{\mathrm{B}}T$ are the Matsubara frequencies, with $n \in \mathbb{Z}$. In this case of a symmetric potential drop, the function $H(V,T)$ is real and writes :

$$H(V,T) = \sin(qVL/\hbar v)\,\frac{2\pi k_{\mathrm{B}}T}{\sinh(\pi k_{\mathrm{B}}T2L/\hbar v)}. \tag{22}$$

The current finally writes :

$$I(\Phi,V,T) = G_0V - \frac{q}{h}\sqrt{R_1R_2}\;\,2\cos(2\pi\Phi/\Phi_0)\,\sin(qVL/\hbar v)\,\frac{2\pi k_{\mathrm{B}}T}{\sinh(\pi k_{\mathrm{B}}T2L/\hbar v)}, \tag{23}$$

which is equivalent to equations (16) and (18) in ref.[5]. The differential conductance writes :

$$G(\Phi,V,T) = G_0 - \frac{q^2}{h}\sqrt{R_1R_2}\;\,2\cos(2\pi\Phi/\Phi_0)\,\cos(qVL/\hbar v)\,\frac{\pi k_{\mathrm{B}}T2L/\hbar v}{\sinh(\pi k_{\mathrm{B}}T2L/\hbar v)}, \tag{24}$$

which forms a checkerboard pattern as a function of field and voltage. At high temperature, the visibility of these oscillations decreases exponentially with a dependence of the form :

$$e^{-\pi k_{\mathrm{B}}T2L/\hbar v} = e^{-4\pi^2 k_{\mathrm{B}}T/E_{\mathrm{Th}}} = e^{-T/T_0}, \tag{25}$$

where $E_{\mathrm{Th}} = hv/L$ is the Thouless energy, which corresponds to the oscillation period $q\Delta V$ versus bias voltage, and T_0 is the fitting parameter of the exponential temperature dependence, which is thus related to the Thouless energy by :

$$4\pi^2 k_{\mathrm{B}}T_0 = E_{\mathrm{Th}} = q\Delta V. \tag{26}$$

Asymmetric potential drop

In case of an asymmetric potential drop (see section XIV) at the two constrictions, the potential energy is $qV^+ = \beta qV$ at the source contact and $qV^- = -\bar{\beta}qV$ at the drain contact, with $\beta = \frac{1}{2}+x$ and $\bar{\beta} = \frac{1}{2}-x$ with the parameter $x \in [-\frac{1}{2},\frac{1}{2}]$ characterizing the asymmetry of the potential drop. The current at finite temperature T and finite voltage V is then given by :

$$I(\Phi,V,T) = \frac{q}{h}\int_{-\infty}^{+\infty} T(E,\Phi)\left(\frac{1}{1+e^{(E-\beta qV)/k_{\mathrm{B}}T}} - \frac{1}{1+e^{(E+\bar{\beta}qV)/k_{\mathrm{B}}T}}\right)\mathrm{d}E \tag{27}$$

Following the same calculations as above now gives the function :

$$H(V,T) = e^{ixqV2L/\hbar v}\sin(qVL/\hbar v)\,\frac{2\pi k_{\mathrm{B}}T}{\sinh(\pi k_{\mathrm{B}}T2L/\hbar v)} \tag{28}$$

which contains a complex phase factor. The current writes :

$$I(\Phi,V,T) = G_0V - \frac{q}{h}\sqrt{R_1R_2}\;\,2\cos(2\pi\Phi/\Phi_0 + xqV2L/\hbar v)\,\sin(qVL/\hbar v)\,\frac{2\pi k_{\mathrm{B}}T}{\sinh(\pi k_{\mathrm{B}}T2L/\hbar v)} \tag{29}$$

which is modified only by the term $xqV2L/\hbar v$ in the cosine function. The differential conductance writes :

$$G(\Phi,V,T) = G_0 - \frac{q^2}{h}\sqrt{R_1R_2}\;\,2\,g(\Phi,V)\,\frac{\pi k_{\mathrm{B}}T2L/\hbar v}{\sinh(\pi k_{\mathrm{B}}T2L/\hbar v)} \tag{30}$$

where the oscillation term :

$$g(\Phi, V) = \cos(2\pi\Phi/\Phi_0 + xqV2L/\hbar v)\,\cos(qVL/\hbar v) - 2x\sin(2\pi\Phi/\Phi_0 + xqV2L/\hbar v)\,\sin(qVL/\hbar v) \tag{31}$$

gives a titled checkerboard pattern as a function of field and voltage for $x \neq 0$. Importantly, these expressions show that the temperature dependence is not affected by the asymmetry of the potential drop at the constrictions. The fitting parameter T_0 of the exponential temperature dependence is still related to the ballistic Thouless energy by $4\pi^2 k_{\mathrm{B}} T_0 = E_{\mathrm{Th}}$.

XVI. ANALYSIS OF THE DOUBLE-CAVITY INTERFEROMETER

In this section we discuss the experiments performed in the coherently-coupled double FP cavity. We first derive the theoretical expression for the transmission for a double cavity and then compare it with our data to show that electron transport remains coherent in the overall device.

The transmission and reflection amplitudes of a Fabry-Pérot interferometer reads:

$$t_{\mathrm{FP}}(\varphi) = \frac{t_1 t_2 e^{i\varphi}}{1 - r_1^{'} r_2 e^{i2\varphi}}, \tag{32}$$

$$t'_{\mathrm{FP}}(\varphi) = \frac{t'_1 t'_2 e^{i\varphi}}{1 - r_1^{'} r_2 e^{i2\varphi}}, \tag{33}$$

$$r_{\mathrm{FP}}(\varphi) = r_1 + \frac{r_2 t_1 t'_1 e^{i2\varphi}}{1 - r_1^{'} r_2 e^{i2\varphi}}, \tag{34}$$

$$r'_{\mathrm{FP}}(\varphi) = r'_2 + \frac{r'_1 t'_2 t_2 e^{i2\varphi}}{1 - r_1^{'} r_2 e^{i2\varphi}}, \tag{35}$$

where 2φ is the Aharonov-Bohm phase accumulated by electrons after one winding in the cavity, t_i (t'_i) the transmission amplitude, and r_i (r'_i) the reflection amplitude of QPC_i for right (left) moving particles.

The total transmission amplitude t_{tot} of two coupled FP cavities can be calculated using the transmission and reflection amplitudes of one FP cavity and the transmission and reflection amplitudes of a third QPC. Thus, using the previous expressions, we have:

$$t_{\mathrm{tot}}(\varphi_1, \varphi_2) = \frac{t_{\mathrm{FP}}(\varphi_1) t_3 e^{i\varphi_2}}{1 - r_{\mathrm{FP}}^{'}(\varphi_1) r_3 e^{i2\varphi_2}}, \tag{36}$$

where $2\varphi_1$ and $2\varphi_2$ are the Aharonov-Bohm phase accumulated by electrons after one winding in the cavity between QPC_1 and QPC_2 and between QPC_2 and QPC_3, respectively.

Using $|t_i|^2 = |t'_i|^2 = T_i$, $|r_i|^2 = |r'_i|^2 = R_i$ and $r'_i = -\bar{r}_i t'_i / \bar{t}_i$ (the overline indicates complex conjugate), we can express the transmission as:

$$T_{\mathrm{tot}}(\phi_1, \phi_2) = \frac{T_1 T_2 T_3}{|1 - \sqrt{R_1 R_2} e^{i\phi_1} - \sqrt{R_2 R_3} e^{i\phi_2} + \sqrt{R_1 R_3} e^{i(\phi_1 + \phi_2)}|^2} = \frac{T_1 T_2 T_3}{D}, \tag{37}$$

where ϕ_1 and ϕ_2 are the Aharonov-Bohm phases acquired when quasiparticles wind into the medium and small cavities respectively (including the phase factor from the reflection amplitudes of the QPCs). The denominator D can be written as :

$$\begin{aligned} D = 1 + R_1 R_2 + R_3 R_2 + R_1 R_3 - 2(1 + R_3)\sqrt{R_1 R_2}\cos(\phi_1) - 2(1 + R_1)\sqrt{R_2 R_3}\cos(\phi_2) \\ + 2\sqrt{R_1 R_3}\cos(\phi_1 + \phi_2) + 2R_2\sqrt{R_1 R_3}\cos(\phi_1 - \phi_2). \end{aligned} \tag{38}$$

In this expression emerges four frequencies of oscillations, namely, ϕ_1, ϕ_2, $\phi_3 = \phi_1 + \phi_2$ and $\phi_4 = \phi_1 - \phi_2$. The terms in ϕ_3 and ϕ_4 in eq. (38), which result from coherent interferences through the two interferometers, does not have the same prefactor. The term in ϕ_3 is proportional to R, whereas the term in ϕ_4 is proportional to the reflection R^2 making it negligible with respect to the former in the weak backscattering limit.

Relating this model to our device geometry, we can ascribe to each of these four Aharonov-Bohm fluxes a coupling to the relevant plunger gates:

$$\phi_1 \simeq \frac{2\pi}{\Phi_0}(\delta A_1 B + A_1 \delta B) = \frac{2\pi}{\Phi_0}(\alpha_1 V_{\mathrm{pg1}} B + A_1 \delta B), \tag{39}$$

$$\phi_2 \simeq \frac{2\pi}{\Phi_0}(\delta A_2 B + A_2 \delta B) = \frac{2\pi}{\Phi_0}(\alpha_2 V_{\mathrm{pg2}} B + A_2 \delta B), \tag{40}$$

$$\phi_3 \simeq \frac{2\pi}{\Phi_0}\left[(\delta A_1 + \delta A_2)B + (A_1 + A_1)\delta B\right] = \frac{2\pi}{\Phi_0}\left[(\alpha_1 V_{\mathrm{pg1}} + \alpha_2 V_{\mathrm{pg2}})B + (A_1 + A_2)\delta B\right], \tag{41}$$

$$\phi_4 \simeq \frac{2\pi}{\Phi_0}\left[(\delta A_1 - \delta A_2)B + (A_1 - A_2)\delta B\right] = \frac{2\pi}{\Phi_0}\left[(\alpha_1 V_{\mathrm{pg1}} - \alpha_2 V_{\mathrm{pg2}})B + (A_1 - A_2)\delta B\right], \tag{42}$$

where A_1 and A_2 are the area of the medium and small cavities, respectively, V_{pg1} and V_{pg2} the plunger-gate voltages that tune these areas and α_1 and α_2 their lever arms.

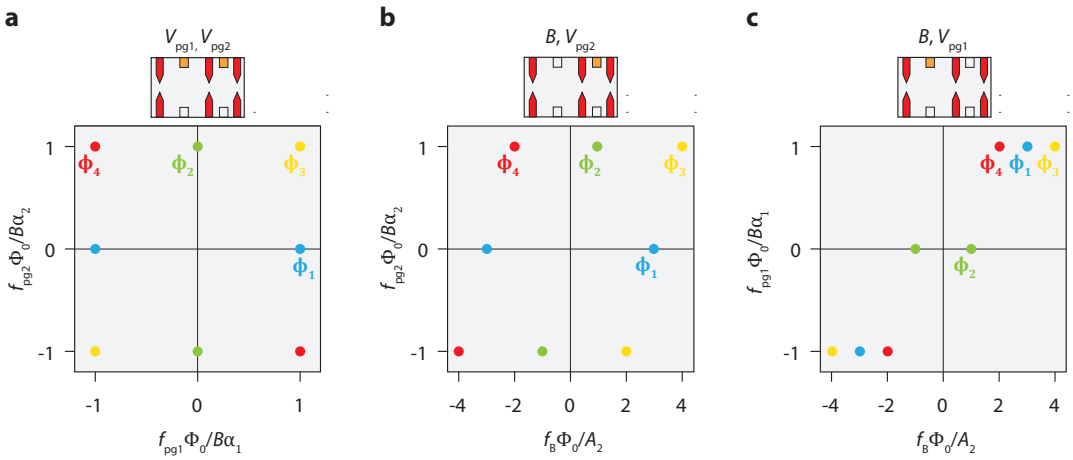

FIG. S19. **Fourier analysis of double QH-FP interferometer. a, b, c,** Positions in reciprocal space of the oscillation frequencies for three different configurations of interferometry experiments (assuming $A_1 = 3A_2$). Each peak is labelled with its Aharonov-Bohm phase. Top schematics depict the active QPCs (red) and plunger gates (orange) in each experiments. The parameters used to tune the Aharonov-Bohm phases in each case are indicated above the corresponding schematic.

In Figure S19 we show the expected frequencies in Fourier space for a coherently-coupled double QH-FP interferometer upon varying both plunger gates (Fig. S19a), or one plunger gate and the magnetic field (Fig. S19b and c). For the former case, the plunger-gate frequencies corresponding to the small and medium interferometers are located on the x and y axis, reflecting the terms ϕ_1 and ϕ_2 in eq. (38), whereas the double interferometer terms ϕ_3 and ϕ_4 that depend on both plunger gates are located on the diagonals. For latter configurations, the frequency of the interferometer without the active plunger gate depends only on B and is thus located at zero plunger-gate frequency on the horizontal axis (ϕ_1 in b and ϕ_2 in c), whereas the frequency of the other interferometer with the active plunger gate, as well as the coupled interferometer frequencies, are located at finite plunger gate frequency.

In Figure S20 we reproduce the data shown in Fig. 4 for the coherently-coupled QH-FP interferometer and add the configuration with V_{pg1} active and magnetic field (Fig. S20c), which provides another confirmation of the presence of the ϕ_3 contribution. The four quadrants of the Fourier amplitudes are shown in order to check the presence of the $\phi_4 = \phi_1 - \phi_2$ frequency. The ϕ_4 frequency, whose expected location is indicated by the red circle in Fig. S20d-f, is clearly present in the configuration of Fig. S20e. Its amplitude is smaller than the amplitude of the ϕ_3 contribution as expected in eq. (38). For the two other configurations, this ϕ_4 frequency is hardly visible. This detailed analysis provides compelling evidence for coherent transport through the three QPCs.

We can furthermore simulate the data by a simplified model that neglects terms in R^2 in eq. (38):

$$\delta R = \delta R_1 \cos(\phi_1) + \delta R_2 \cos(\phi_2) + \delta R_3 \cos(\phi_3). \tag{43}$$

Using the experimental Fourier amplitudes for the parameters δR_1, δR_2 and δR_3 we obtain the resistance maps shown in Fig. S20g-i that reproduce the experimental maps in Fig. S20a-c with excellent fidelity.

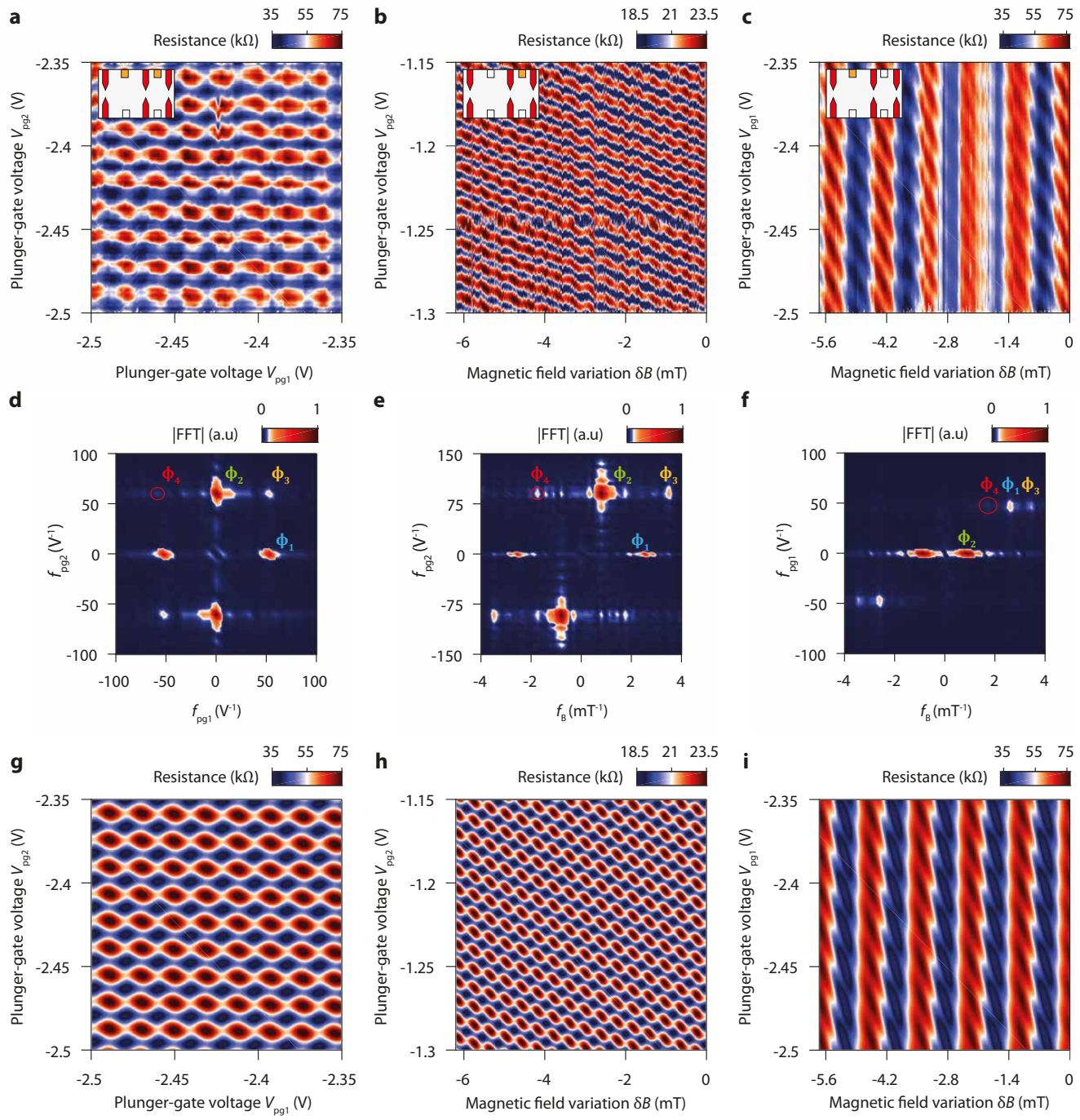

FIG. S20. **Coherently-coupled double QH-FP interferometer. a,** Diagonal resistance versus plunger-gate voltages V_{pg1} and V_{pg2} (outer edge channel interfering, $B = 14$ T). **b,** Diagonal resistance versus magnetic field variation δB and plunger-gate voltage V_{pg2} (inner edge channel interfering, $B = 14$ T). **c,** Diagonal resistance versus magnetic field variation δB and plunger-gate voltage V_{pg1} (outer edge channel interfering, $B = 14$ T). The inset schematics in a, b and c indicate the active QPCs (in red) and plunger gates (in orange) for the respective measurements. a and b are identical to the Fig. 4c and 4d of the main text. **d, e, f,** Four-quadrant Fourier amplitude of the resistance oscillations displayed respectively in a, b and c in their respective reciprocal space. The peaks corresponding to the different Aharonov-Bohm phases are identified in each case. **g, h, i,** Numerical simulations reproducing the experiments shown respectively in a, b and c with eq. (43). The parameters (δR_1, δR_2, δR_3) are (0.66, 1, 0.18) in g, (0.64, 1, 0.22) in h, and (0.19, 1, 0.11) in i.